Post-forming Room Temperature Brittle Fracture in a High-Strength Low-Alloy Steel Sheet After Various Forming Modes

Philippe L. Charpentier

The effects of various sheet forming modes on the post-forming room temperature fracture behavior of a 550-MPa yield strength high-strength low-alloy (HSLA) steel are investigated. In-plane biaxial stretching, plane strain (cold rolling), uniaxial tension, cylindrical cup drawing, and in-plane compression (IPC) are examined up to a von Mises effective prestrain ε_{eff} = 0.7. Most of the results pertain to sub-size Charpy-type impact specimens prepared from the prestrained material. After sufficiently large prestrains, the fracture behavior is highly anisotropic. Low-energy fracture modes, namely cleavage and intergranular fracture, occur after all modes of prestraining along plane directions that are perpendicular to the principal compressive prestrain. These planes are parallel to the sheet surface after biaxial stretching and cold rolling and correspond to brittle splits extending into the primary, ductile fracture surface. After cup drawing, the brittle planes are oriented perpendicular to the circumferential compressive prestrain. This results in very low energy fractures propagating in the length direction of a fully drawn cup. After in-plane compression, brittle fracture occurs along planes that are perpendicular to the compression direction. The fracture toughness for a crack propagating along such a plane after IPC to ε_{eff} = 0.38 was very low (12.7 MPa $\sqrt{m}$), much lower than in the undeformed condition (247 MPa$\sqrt{m}$). Changes in grain shape and in crystallographic texture caused by the various prestraining modes, as well as the microstructural damage at non-metallic inclusions and carbides, are examined to try to understand the fracture behavior.

1. Introduction

1.1 Background

Sheet metal parts, which are used in many industries, are often produced by cold forming. The post-forming mechanical properties are different from those in the as-received material since, in general, there is an increase in strength and a decrease in ductility during cold forming. In addition, some sheet forming operations produce a marked mechanical anisotropy.

Several investigations have been conducted in the past on the effect of one or several sheet forming modes (primarily uniaxial tension and biaxial stretching) on the post-forming flow behavior in steel sheets (Ref 1-5). The influence of deep drawing, which, unlike the two previous modes, involves a compressive prestrain in the plane of the sheet, on flow (Ref 6-8) and on fracture (Ref 6, 9, 10) of steel sheets has also received some attention. This mode of prestraining was found to result

in: (1) large post-forming flow anisotropy (Ref 6), due in part to the Bauschinger effect and in part to crystallographic texture formation (Ref 7), and (2) room temperature brittle fracture characterized by a fracture path parallel to the drawing direction.

This type of brittle fracture exhibits similarities with the "compression embrittlement" extensively studied in the 1950s and 1960s by Mylonas and his coworkers (Ref 11-13). These authors showed that compressive prestrains of sufficient magnitude, obtained by axial compression of cylindrical bars or notched plates, caused a severe loss of ductility and a sudden decrease in fracture stress during subsequent tension in the direction of the prior compressive strain.

The microstructural mechanisms of this embrittlement in Armco iron were investigated by Brenneman and Rogers (Ref 14, 15). The embrittlement, which only occurred in notched tension tests (not in smooth specimens), was found to correlate with the formation of transverse microcracks around oxide inclusions during longitudinal compression and with the development of a <100> fiber texture.

Brittle fractures have also been seen in service in more complex parts involving some drawing deformation, particularly when notches were present, as for example in sheared edges (Ref 6).

All these investigations have led to the general recognition of the importance of post-forming properties in predicting the service performance of formed parts, particularly in the automotive industry (Ref 16). Issues such as crash worthiness, dent resistance, and fatigue resistance (Ref 17) depend critically on such properties.

The desire to avoid post-forming embrittlement has resulted over the years in many investigations [e.g., (Ref 18-25)] that

Philippe L. Charpentier—retired from Bettis Atomic Power Laboratory.

Philippe L. Charpentier, Bettis Atomic Power Laboratory, West Mifflin, PA; and 3133 Annapolis Avenue, Pittsburgh, PA 15216. Contact e-mail: philcharp@verizon.net.

have focused on ways to manipulate the steel microstructure and mill processing to improve the resistance to what is usually termed secondary work embrittlement in these investigations. This metallurgical line of research is quite valuable, of course, but totally distinct from the one pursued in the present work which is more mechanically focused. However, it must be pointed out that the two approaches intersect because one of the tests typically used to evaluate secondary work embrittlement consists of loading the periphery of a deep drawn cup in a drop weight type of test. It was observed (Ref 20) that, for a given microstructure, the susceptibility to embrittlement, measured by this test, increases as the drawing ratio increases. This indicates that there is an effect not only of metallurgical variables but also of the level of prior strain (circumferential compressive strain in the cup) on embrittlement. It is this effect of prior strain that is investigated in the present work, in greater detail than previously done in the literature. It should be noted that, as pointed out in Ref 16, the embrittlement due to cold work alone described in early investigations (Ref 9-15) "has been largely forgotten in modern metallurgical analysis." Indeed, there is a dearth of recent investigations on this topic.

1.2 Goal of Investigation

The primary goal of this investigation was to examine the post-forming fracture behavior of a HSLA steel sheet, and particularly its anisotropy aspects, under relatively severe conditions (notch constraint, high strain rate) and for the widest possible range of sheet forming modes (prestraining) achievable in the laboratory. Another goal was to relate the fracture behavior to the changes in microstructure and crystallographic texture produced by the various types of prestrains.

2. Material and Experimental Procedures

2.1 Material

The material was a commercial, vanadium bearing, rare-earths treated 550 MPa minimum yield strength HSLA steel sheet (VAN-80 or V-N steel)) obtained from the plant in the hot-rolled, cut-to-length, pickled-and-oiled condition. Its nominal thickness was 3.17 mm. The as-received chemical composition, in weight percent, was: 0.11 C, 1.3 Mn, 0.5 Si, 0.010 S, 0.010 P, 0.08 Al, 0.015 N, 0.12 V, 0.024 Ce. The as-received tensile properties are shown in Table 1.

2.2 Prestraining

Prestraining was performed using 5 different modes of deformation: in-plane balanced biaxial stretching, plane strain (cold rolling), uniaxial tension, cylindrical cup drawing, and in-plane compression, a laboratory forming technique, previously described in detail (Ref 7), designed to produce a strain state

similar to that present in the flange of a partially drawn cylindrical cup but without the presence of strain gradients to make it easier to obtain test specimens.

These five deformation modes can be characterized by the ratio ρ of the two principal surface strains in the plane of the sheet, $\rho = \varepsilon_2/\varepsilon_1$, where ε_1 and ε_2 are the major and the minor principal surface strains, respectively. In this investigation, ρ varied from $\rho = 1$ for balanced biaxial stretching, to $\rho = 0$ for plane strain cold rolling and $\rho \approx -0.46$ for uniaxial tension (value calculated using the r-value of 0.86 in the longitudinal direction). For cup drawing, the measured values of ρ on all the test specimens obtained from the cup flanges ranged from -1.25 to -1.75, with an average value $\rho_{avg} = -1.55$. For in-plane compression, ρ varied with the amount of compression, ranging from -1.8 for the larger effective strains to -2.6 for the smaller ones. This variation was a result of the lateral elastic deformation of the die under various amounts of compression (see Sect. 2.2.4). The strain paths corresponding to the five deformation modes are represented in Fig. 1.

2.2.1 Balanced Biaxial Stretching (BBS). The method developed by Marciniak et al. (Ref 26) was used to produce flat samples exhibiting balanced biaxial stretching. The method, which uses a cylindrical flat bottom punch and an auxiliary blank, containing a circular hole, between the punch and the sheet to be stretched, is based on differential friction and requires low friction between the punch and the auxiliary blank but high friction between the auxiliary blank and the work-piece. The punch and die dimensions were as follows: punch diameter 127 mm, punch nose radius 25.4 mm, die diameter 158.7 mm, die draw radius 25.4 mm. The hole in the auxiliary blank was reamed to a diameter of 35 mm and polished smooth with fine emery paper. A 0.075-mm-thick polyethylene sheet was used as lubricant between the punch and the auxiliary blank. There was no lubrication between the two blanks, which were thoroughly cleaned and degreased before forming. A 2.54-mm circular grid pattern was applied to the workpiece by a photographic process. Under these conditions, using a 150-ton double action HPM press, flat, 76-mm-diameter samples, equibiaxially stretched and essentially free from strain gradients, were produced with strains up to $\varepsilon_1 = \varepsilon_2 = 0.35$ (von Mises effective strain $\varepsilon_{eff} = 0.7$).

2.2.2 Cold Rolling and Uniaxial Tension. A two high laboratory cold rolling mill with 203 mm rolls was used to produce two sets of plane strain samples up to $\varepsilon_{eff} = 0.7$: one by rolling in the hot rolling direction (HRD) and the other by rolling perpendicular to HRD. For uniaxial tension, large specimens parallel to the hot rolling direction were used to produce deformed material up to $\varepsilon_{eff} = 0.33$ (in the neck), i.e., well beyond the uniform elongation.

2.2.3 Cup Drawing. Partially drawn cylindrical cups exhibit a circumferential compressive strain in the flange. However, the effective strain level achievable in a cup flange

Table 1 As-received tensile properties

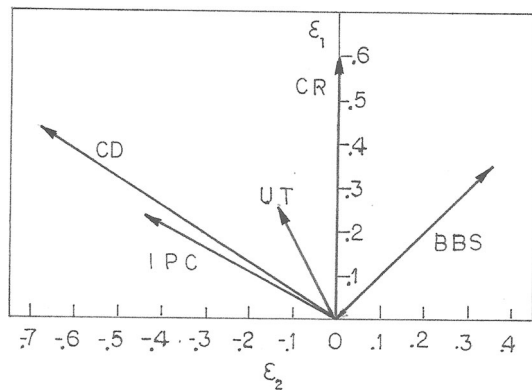| Testing direction	Yield strength, MPa	Tensile strength, MPa	Yield point elongation, %	Elongation at max. load, %	Total elongation in 50.8 mm, %	Plastic strain ratio, r
Longitudinal	584	714	1.4	13.1	21.8	0.86
Transverse	595	704	1.25	10.8	18.8	0.93
45° diagonal	588	701	1.55	11.9	20	1.06

Fig. 1 Strain paths for the five deformation modes: balanced biaxial stretching (BBS), cold rolling (CR), uniaxial tension (UT), cup drawing (CD), and in-plane compression (IPC). Arrowheads correspond to the maximum prestrain achieved in each mode

wide enough to extract a miniature test specimen is quite limited. For example, when the 3.17-mm-thick steel investigated here was partially drawn into a 101.6-mm-diameter cup, the largest von Mises effective strain obtainable in a 12.7-mm gage length tension specimen aligned in the circumferential direction was approximately $\varepsilon_{\text{eff}} = 0.35$. This value is well below the maximum strain present at the edge of a fully drawn cup ($\varepsilon_{\text{eff}} \approx 0.7$, corresponding to the Limiting Drawing Ratio for this steel, LDR ≈ 2). Since it is desirable to measure the post-forming properties corresponding to the largest strains that can occur, a modified cup drawing technique was used, in addition to the standard full thickness technique, to achieve this goal.

In this technique, described in detail earlier (Ref 7), circular blanks of fixed diameter (241 mm, much larger than the critical blank diameter for the full thickness steel) were reduced in thickness at their periphery by machining. This thickness reduction decreased the drawing load required to draw the flange without changing the load carrying capacity of the cup wall base where full thickness was maintained. Hence, an artificially large critical blank diameter was attained. The prethinned blanks were drawn into cups of various depths, thus producing various flange widths and therefore various strain levels in the flanges.

2.2.4 In-Plane Compression (IPC). This technique, also previously described in detail (Ref 7), was devised to produce relatively large samples exhibiting a strain state like that in a cup flange but without the radial strain gradients. In this technique, a rectangular sheet sample of length $L = 125$ mm, height h (variable), and thickness $t = 2.79$ mm is compressed on edge with a punch in a narrow channel die. The sample is surface ground on all sides and a photogrid is applied. The compression force is parallel to the plane of the sheet, hence the name in-plane compression (IPC). The sample is coated with a MoS_2 paste and wrapped in a polyethylene sheet to provide lubrication. A compressed sample is shown in (Ref 17). The longitudinal strain, $\varepsilon_l > 0$, is equivalent to the radial strain in a cup flange, and the compressive strain, $\varepsilon_c < 0$, is equivalent to the circumferential strain. The thickness strain, ε_{th}, is positive, both in IPC, because of the lateral elastic deformation of the die during the compression, and in cup drawing, because the hold-

down force is insufficient to prevent thickening of the blank. All samples are compressed to the same final height, and the strain level in the deformed sample is controlled by varying the initial height, h. Strains up to $\varepsilon_{\text{eff}} = 0.45$ were obtained in the center sections of some samples. Two sets of samples were produced: one set parallel to the hot rolling direction and the other perpendicular to HRD.

2.3 Test Specimens

2.3.1 Charpy-Type Specimens. Sub-size Charpy-type specimens were machined from the 5 types of deformed material with various levels of prestrain. The specimens were oriented parallel to the two principal surface strains and either parallel or perpendicular to the hot rolling direction. This produced four testing orientations after cold rolling, cup drawing, and in-plane compression but only two testing orientations after balanced biaxial stretching (because of the prestraining symmetry) and after uniaxial tension (because the only prestraining was parallel to HRD). The Charpy specimens had standard dimensions (ASTM standard E23-07a) except for the thickness, which was the as-prestrained thickness, and for the geometry of the notch (60° angle and 0.025 mm root radius, i.e., 10 times smaller than in the standard geometry). This was chosen to enhance the sensitivity of the test to differences in fracture behavior.

2.3.2 Tensile Specimens. Miniature tensile specimens with a 12.7 mm gage length, 3.17 mm width, and as-prestrained thickness were also obtained for selected prestrains from the 5 types of deformed material in the same orientations as the Charpy specimens.

2.3.3 Fracture Toughness Specimen. The fracture toughness after in-plane compression was measured for a crack propagating in a plane perpendicular to the compression direction, using a fatigue precracked Charpy-type specimen loaded in three point slow bending. The specimen was machined from material compressed to $\varepsilon_{\text{eff}} = 0.39$. The fatigue precrack length was 3.3 mm (average of two measurements on the specimen surfaces) and the specimen thickness 3.32 mm.

2.4 Mechanical Testing

2.4.1 Charpy Specimens Testing. Charpy impact energies were measured in the standard fashion (ASTM E23-07a) using an initial impact velocity of 3.35 m/s and pendulum potential energies of 34 Nm in most cases and 68 Nm when necessary. The measured impact energies were converted to "specific impact energies," i.e., measured impact energy divided by specimen thickness to take into account the variation in as-prestrained thickness. The specific impact energies were plotted as a function of von Mises effective prestrain for all deformation modes.

2.4.2 Tensile Specimens Testing. Tensile specimens corresponding to selected effective prestrains were tested to fracture for each of the five deformation modes. Their fracture appearance was compared to that of the Charpy specimens and used in the interpretation of the overall fracture behavior.

2.4.3 Fracture Toughness Testing. The fatigue precracked Charpy specimen was loaded in a three point bending jig in an Instron testing machine at a crosshead speed of 0.02 mm/s. The load versus time curve was recorded up to fracture.

2.5 Fractography, Metallography, and Crystallographic Texture Measurements

The fracture surfaces of fractured specimens were examined under low power optical stereomicroscopy and by scanning electron microscopy (SEM) to determine the microscopic fracture modes. In some cases, etched metallographic cross sections perpendicular to the fracture surfaces were also examined by optical microscopy or SEM to look at the microstructure immediately below the fracture surfaces.

The effect of cold work under the various modes of deformation on the changes in grain shape and on the non-metallic inclusion integrity was examined in metallographic cross-sections both optically and by SEM.

Finally, crystallographic texture measurements were conducted on prestrained samples after BBS, cold rolling, and IPC. First, ordinary X-Ray pole figures were obtained to establish the nature of the textures. These measurements were made at the quarter thickness depth. Then, diffraction peak intensities (inverse pole figures) of low index planes were measured for the three modes of deformation.

3. Charpy Impact Results. Macroscopic Fracture Appearance in Charpy and Tensile Specimens. Fracture Toughness Test Results

3.1 Balanced Biaxial Stretching and Cold Rolling Results

3.1.1 Specific Impact Energies After BBS and Cold Rolling. The specific impact energy decreased gradually with increasing prestrain. After biaxial stretching, the initial anisotropy (longitudinal versus transverse energy in the as-received sheet) remained essentially unchanged with increasing prestrain (Fig. 2), reflecting the axisymmetric nature of the deformation. Some specimens, aged for 6 months at room temperature after BBS, showed no effect of aging on impact energy. After cold rolling, the anisotropy increased with prestrain when cold rolling was parallel to HRD. When cold rolling was perpendicular to HRD (cross rolling), the initial anisotropy was gradually eliminated and then reversed (Fig. 2).

3.1.2 Macroscopic Fracture Appearance After BBS and Cold Rolling. Two types of fracture appearance, *type I and type II*, were observed after BBS and after cold rolling. These two types are illustrated in Fig. 3, and their occurrence is noted in Fig. 2 for the various specimens. *Type I* was a predominantly slant fracture that occurred after low prestrains. *Type II* was similar to type I in that it contained large portions of slant fracture, but, in addition, there was an increasing tendency to form splits parallel to the plane of the sheet as the prestrain increased (Fig. 3). The splits tended to be concentrated in a band centered at the mid-thickness of the sheet. There were clearly visible chevrons, indicating successive positions of the crack front. The frequency and severity of the splits did not appear to be significantly different for BBS or cold rolling.

3.2 Cup Drawing Results

3.2.1 Specific Impact Energies After Cup Drawing. After cup drawing, a totally different fracture behavior was observed, in terms of both impact energy and fracture appearance. The changes in impact energy with prestrain are shown in Fig. 4 for circumferential and radial specimens oriented either parallel or perpendicular to HRD. These specimens, taken from prethinned blank cup flanges, ranged in thickness from 1.8 to 2.1 mm.

In the circumferential specimens, i.e., specimens with radial cracks, i.e., cracks perpendicular to the compressive prestrain, the impact energy decreased gradually at first with increasing prestrain, but then suffered a severe drop when the prestrain reached a critical value. This critical value was dependent on the orientation of the specimens with respect to HRD. It was lower when the radial crack propagated parallel to HRD ($\varepsilon_{crit} \approx 0.32$) rather than perpendicular to HRD ($\varepsilon_{crit} \approx 0.44$).* This result reflects the initial fracture anisotropy in the as-received material. Beyond the critical prestrains, the impact energies were very low and decreased only gradually with increasing prestrain.

In the radial specimens, the impact energy initially decreased with increasing prestrain at approximately the same rate as in the circumferential specimens, but then increased with prestrain and showed large scatter. As a result, the impact energy anisotropy caused by this type of cold work was very large, i.e., approximately a tenfold difference between circumferential and radial orientations for a given prestrain beyond the critical prestrain.

3.2.2 Macroscopic Fracture Appearance After Cup Drawing. Five types of fracture appearance (types I, III, IV(A), IV(B), V), indicated for each specimen in Fig. 4, were observed after cup drawing.

In the circumferential specimens, *type I*, occurring after low prestrains, was the same as described earlier in Sect. 3.1.2. *Type III* fracture, present in all specimens above the critical prestrains, was a fully square brittle fracture exhibiting a straight crack path along the radial direction (Fig. 5(a) and (b)). *Type V* fracture occurred in the transition zone near the critical prestrains. This fracture started as a slant fracture in the radial direction and ended as a square brittle fracture in the same direction (Fig. 5(c) and (d)).

In the radial specimens, *type I* fracture was observed at low prestrains. In *Type IV(A)* fracture (Fig. 6(a) and (b)), which occurred after high prestrains, the crack was diverted away from the intended direction of propagation shortly beyond the notch and assumed a sideway path reflecting the anisotropy produced by the directional cold work. This portion of the fracture was square and brittle in appearance. The crack then followed an irregular path exhibiting abrupt changes in direction accompanied by changes from square fracture to slant fracture and back. In the radial specimens with intermediate prestrains, *type IV(B)* occurred. This started as a slant fracture in the circumferential direction, then the crack proceeded as a square fracture in the radial orientation (Fig. 6(c) and (d)).

3.3 In-Plane Compression (IPC) Results

3.3.1 Specific Impact Energies After IPC. These data are presented in Fig. 7 in a way that permits direct comparison with the cup drawing results, i.e., the data points for specimens

---

*In circumferential specimens obtained from full thickness cups (3.3-3.4 mm), the critical prestrains were significantly smaller, i.e., $\varepsilon_{crit} \approx 0.13$ and $\varepsilon_{crit} \approx 0.22$, for specimens perpendicular and parallel to HRD, respectively.
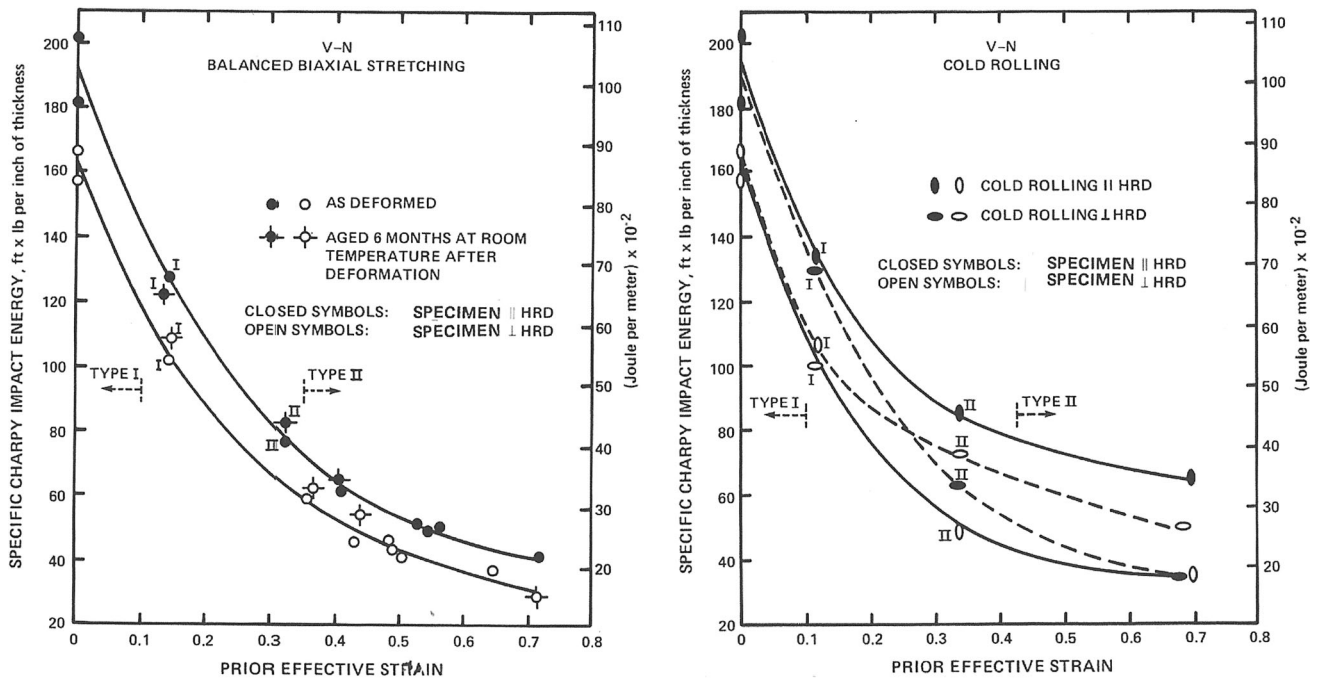
Fig. 2 Specific Charpy V-notch impact energy in J/m and ftlb/in after balanced biaxial stretching and cold rolling (Ref 6). Roman numerals indicate macroscopic fracture types. *HRD* hot rolling direction
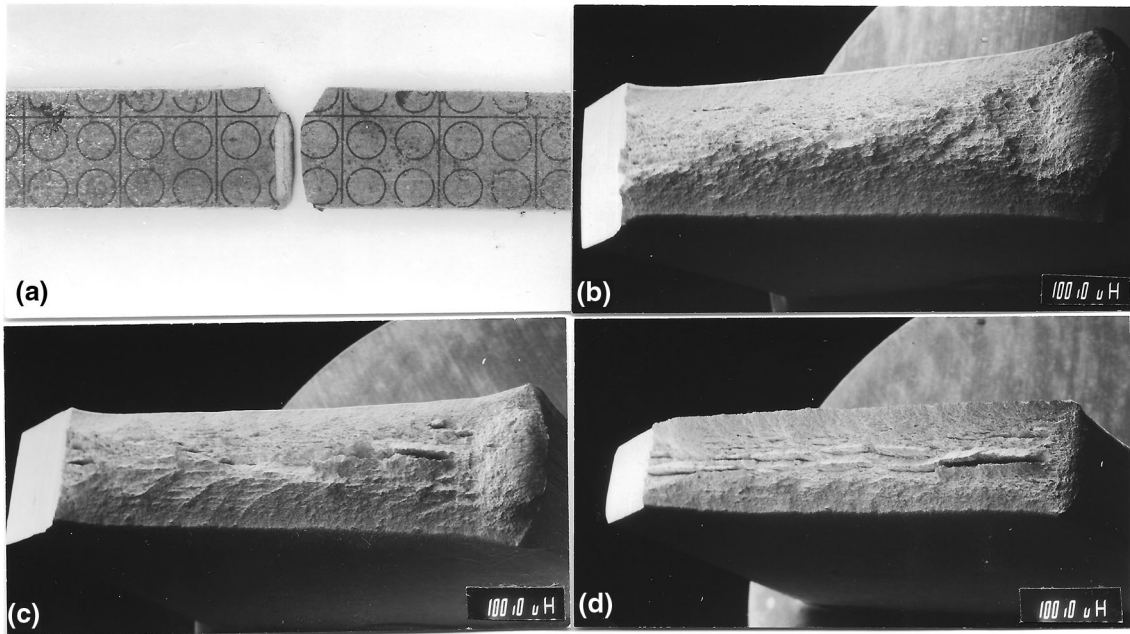

Fig. 3 Macroscopic fracture appearance and fracture types after balanced biaxial stretching (BBS) and cold rolling. Type I: slant fracture. Type II: slant fracture plus splits. (a) Fracture path in types I and II. (b) Type I, $\varepsilon_{eff} = 0.14$. (c) Type II, $\varepsilon_{eff} = 0.35$. (d) Type II, $\varepsilon_{eff} = 0.71$. The specimens shown here were all prestrained by BBS

parallel and perpendicular to the IPC direction but having the same orientation with respect to HRD are grouped together in the same plot.

For specimens parallel to the IPC direction, i.e., cracks in a plane perpendicular to the IPC direction (dashed lines in Fig. 7), the fracture behavior was similar to that for cup drawn specimens of equivalent orientation (circumferential speci-

mens). Namely, after a gradual energy decrease with increasing prestrain, an abrupt drop or transition region was observed, followed by a slow decrease. The critical strains corresponding to the impact energy drop were $\varepsilon_{crit} \approx 0.2$ and $\varepsilon_{crit} \approx 0.25$ for specimens perpendicular and parallel to HRD, respectively, much smaller than after cup drawing. The IPC specimens in the
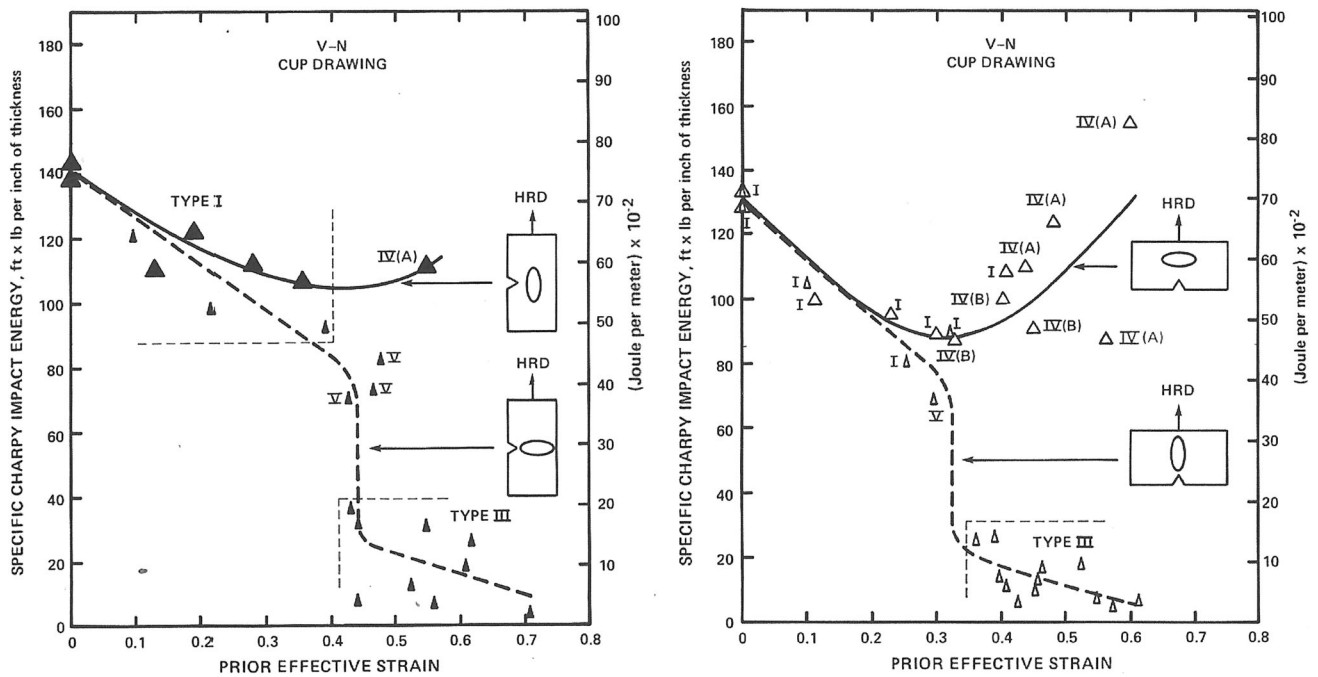
Fig. 4 Specific Charpy V-notch impact energy in J/m and ftlb/in after cup drawing (prethinned blanks) (Ref 6). Solid curves and dashed curves correspond to radial and circumferential specimens, respectively. Ellipses shown inside the specimens indicate the circular grid shape after cup drawing. Closed and open symbols represent specimens //and ⊥ HRD, respectively. *HRD* hot rolling direction. Roman numerals indicate macroscopic fracture types
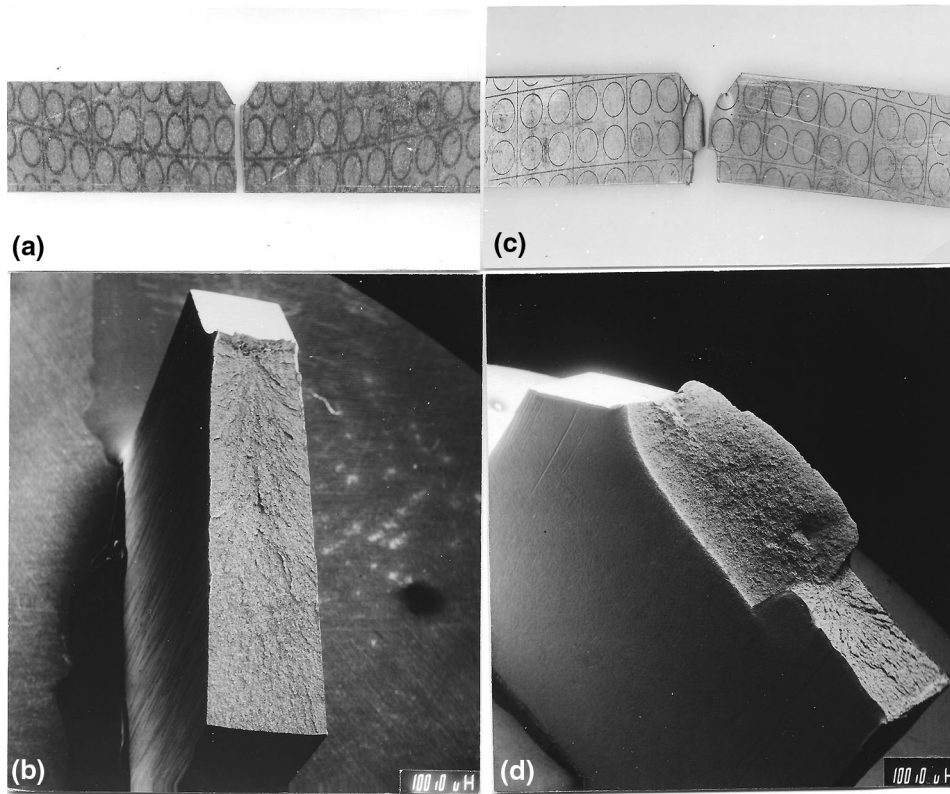

Fig. 5 Circumferential Charpy specimens after cup drawing: macroscopic fracture types and appearance. Type III fracture occurs beyond the impact energy transition, type V within the transition. (a) Type III (ε_{eff} = 0.41) showing straight path of square fracture. (b) Type III (ε_{eff} = 0.6) showing square fracture surface. (c) Type V (ε_{eff} = 0.3) showing mixed path of slant fracture followed by square fracture. (d) Type V (ε_{eff} = 0.47) showing slant, then square fracture surfaces
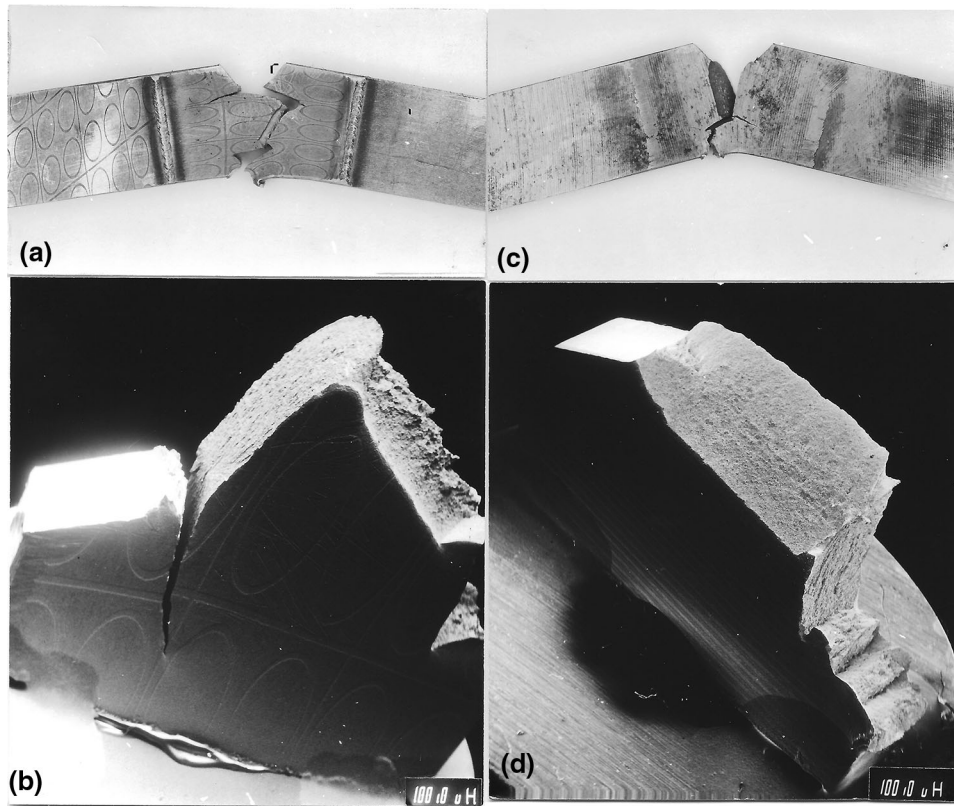
Fig. 6 Radial Charpy specimens after cup drawing: macroscopic fracture types and appearance. (a, b) High prestrain, type IV(A), $\varepsilon_{eff} = 0.6$, specimen $\perp$ HRD. (c, d) Low prestrain, type IV(B), $\varepsilon_{eff} = 0.4$, specimen $\perp$ HRD

transition region were thicker (3.1-3.2 mm) than the specimens in the transition region after cup drawing (1.8-2.1 mm).

For specimens perpendicular to the IPC direction, the impact energy behavior was similar, i.e., it also exhibited an abrupt drop for critical prestrains only slightly larger than those above. Thus, this behavior was different from that observed after cup drawing for equivalently oriented specimens.

3.3.2 Macroscopic Fracture Appearance After IPC. In specimens parallel to the IPC direction, the fracture appearance was similar to that after cup drawing in circumferential specimens, i.e., fractures *of types I, III, and V*, described in Sect. 3.2.2, were observed, depending on prestrain level. Above the critical prestrains, all specimens exhibited *type III*, brittle, square fractures with straight cracks propagating in a plane perpendicular to the compressive prestrain.

In specimens perpendicular to the IPC direction, the fracture path and appearance were different from those after cup drawing in radial specimens at high prestrains. A striking new fracture type, *IV(C)*, exhibiting an unusual fracture path, occurred beyond the critical prestrains. Near the notch, this fracture followed the usual, expected path over a very short distance (about 1 mm) and was fibrous. Then, an abrupt, sideway change in direction occurred which increased in magnitude with increasing prestrain, from 46° for $\varepsilon_{eff} = 0.25$ to 72° for $\varepsilon_{eff} = 0.72$. Additional changes in direction took place across the specimen width. All along the fracture path (except very near the notch), the fracture was essentially square and macroscopically brittle in appearance, although small shear lips were sometimes present along the specimen surfaces (Fig. 8).

3.4 Uniaxial Tension Results (Impact Energies and Fracture Types)

In uniaxial tension, a compressive prestrain, oriented at 90° to the applied tensile stress, is produced in the plane of the sheet, as in cup drawing and IPC. This prestrain, however, occurs under tensile stresses rather than compressive stresses as in cup drawing and IPC.

The impact energy results, however, were similar in that type III brittle fracture was observed beyond a critical prestrain ($\varepsilon_{crit} \approx 0.3$) in Charpy specimens parallel to the compressive prestrain (crack path perpendicular to the compressive prestrain). For lower prestrains, the fracture appearance was either of type I or of type V, as noted in Fig. 9.

3.5 Fracture Toughness Results

The load versus time curve was almost linear. Brittle fracture occurred very quickly after the beginning of load application, i.e., after a crosshead motion of only 0.38 mm and at a load P_{max} of only 407 N. The fracture was fully square and macroscopically brittle in appearance.

An estimate of the "degree of brittleness" can be obtained by comparing the fracture load (407 N) with the load required to cause general yielding in the specimen net section. This load is given by Ref 27, 28:

$$P_{GY} = \sigma_{yield} \times B \times (W - a)^2 \Big/ 2.85 \times W$$

where σ_{yield} is the yield strength of the material, B and W the specimen thickness and width, respectively, and $(W - a)$ the
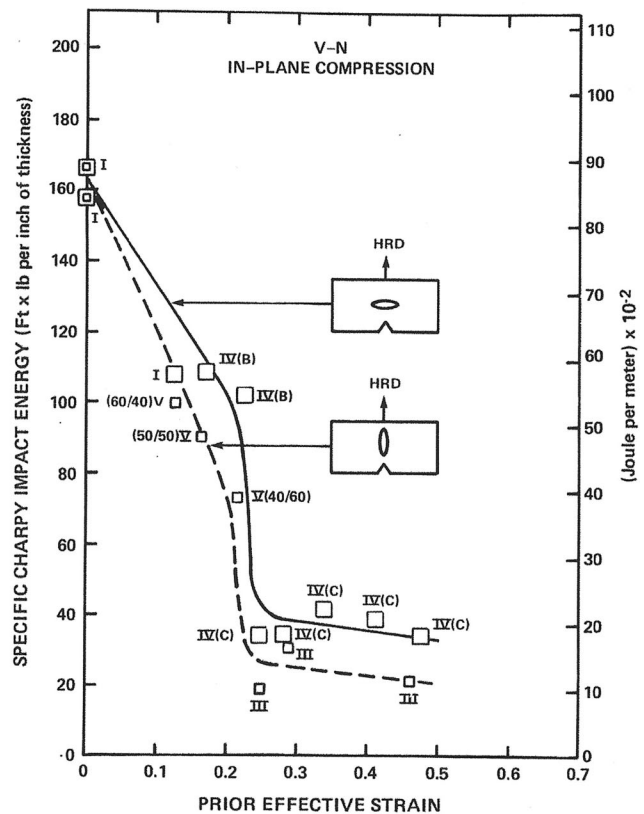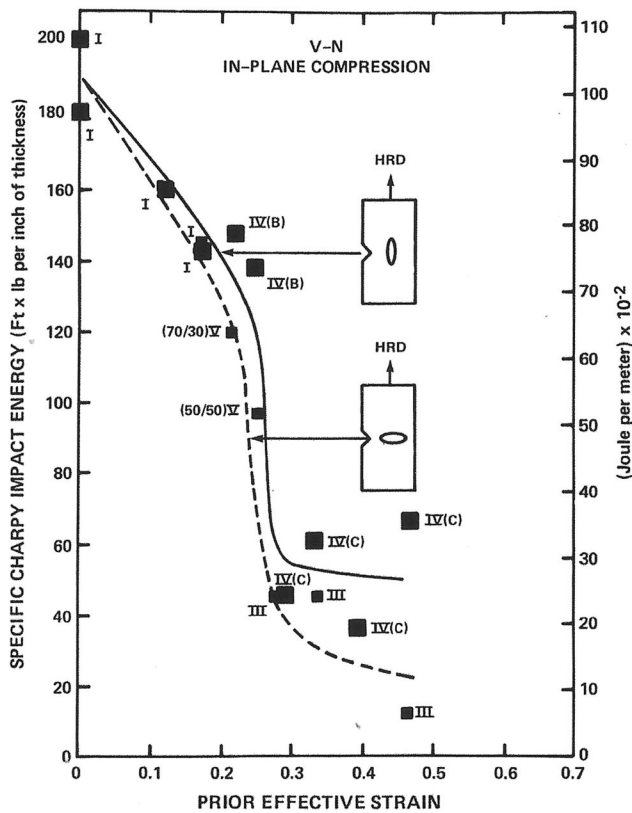
Fig. 7 Specific Charpy V-notch impact energy in J/m and ftlb/in after in-plane compression. Solid curves and dashed curves correspond to specimens ⊥ and // to the compressive prestrain, respectively. Closed and open symbols represent specimens //and ⊥ HRD, respectively. *HRD* hot rolling direction. Roman numerals indicate fracture types and numbers in parentheses (70/30) represent the percentages of slant and square fracture (70% slant, 30% square) in specimens exhibiting type V fracture

ligament width under the precrack. Using the value of yield strength in the direction of the largest principal stress at the crack tip, obtained from separate tensile testing for this prestrained material (614 MPa), and the values of B, a, and W given in previous sections, we obtain:

$$P_{GY} = 1,575 \text{ N}$$

Thus, the fracture load is about 3.9 times smaller than the general yielding load, which indicates a high degree of brittleness.

As a first step in the calculation of fracture toughness, the load at fracture was used to calculate an upper bound value of the fracture toughness, K_{IX} (Ref 29)

$$K_{IX} = 1.5 \, P_{max} SYa^{1/2}/BW^2$$

where S is the support span of the specimen and Y is a polynomial function of a/W defined in Ref 29. We obtain:

$$K_{IX} = 14.5 \, \text{MPa}\sqrt{m}.$$

The validity criteria adopted in ASTM standard E399-17 to ensure that Linear Elastic Fracture Mechanics (LEFM) is applicable to this test include conditions on crack geometry (length, straightness, and orientation) and specimen thickness.

The crack length must satisfy the condition: $0.45 < a/W < 0.55$, where the precrack length is now determined as the average of 5 measurements across the crack front rather than 2 measurements on the specimen surfaces. This new precrack

length, obtained from measurements after fracture, is 3.4 mm, which gives $a/W = 0.54$.

The crack straightness criterion requires that the deviation of the crack front from the calculated average (3.4 mm) be less than 5% in the central portion (3 positions) and less than 10% at the edges. In the present case, the deviation was less than + 0.8% in the central portion, and less than − 7.1% at the edges.

The last crack requirement, i.e., that the plane of the crack be within 10° from the plane of symmetry of the notch, was also satisfied.

The specimen thickness requirement is that:

$$B \geq 2.5 \, (K_{IX}/\sigma_{yield})^2$$

With the previous values of K_{IX} and of yield strength, we find $B \geq 1.39$ mm, which is easily satisfied (specimen thickness 3.32 mm).

The load time curve, which approximates the load versus crosshead displacement and the load versus specimen deflection, was used to calculate an approximate plane strain fracture toughness value, K_Q, using the load obtained with a secant of 5% lower slope than the elastic line, according to ASTM E 399.

This load was found to be 364.5 N, and the corresponding calculated value of K_Q was:

$$K_Q = 12.7 \, \text{MPa}\sqrt{m}.$$

For comparison, the fracture toughness of nominally the same steel in the as-received, hot-rolled condition, approxi-
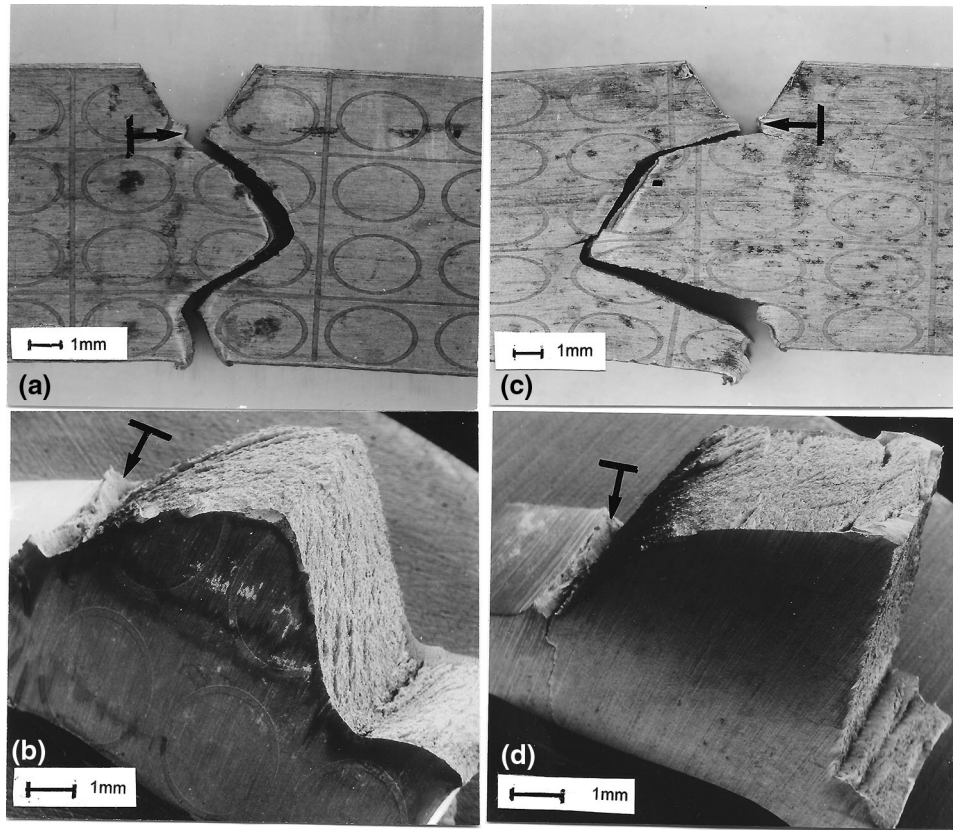
Fig. 8 Two Charpy specimens perpendicular to the compressive prestrain after in-plane compression (equivalent to radial specimens after cup drawing). Both specimens exhibit type IV(C) fracture, are // HRD, and represent prestrains beyond the impact energy transition. (a, b) ε_{eff} = 0.28. With this low prestrain, moderate deviation of the fracture path occurs. (c, d) ε_{eff} = 0.47. With this high prestrain, greater deviation of the fracture path is observed. Arrows indicate small region of fibrous fracture near the notch
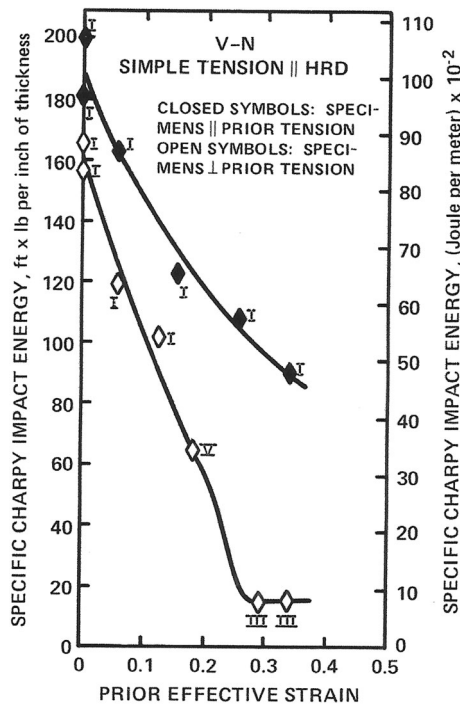
Fig. 9 Specific Charpy V-notch impact energy in J/m and ftlb/in after uniaxial tension. Roman numerals indicate fracture types. *HRD* hot rolling direction

mately 7.6 mm thick, ranged from K_C = 247 to 324 MPa√m (Ref 30). For that material and that thickness, plane stress conditions prevailed and the fracture toughness was obtained from an R-curve analysis.

3.6 Macroscopic Fracture Appearance in Post-forming Tensile Specimens

The fracture appearance of tensile specimens taken from material deformed to relatively large prestrains by BBS, cold rolling, cup drawing, and IPC is presented here, because, as will be seen later, these results will help in interpreting the overall fracture behavior.

Figure 10 shows longitudinal splits in two fractured tensile specimens: one from IPC material (ε_{eff} = 0.47) and the other from cold-rolled material (ε_{eff} = 0.6). In Fig. 10(a) (IPC specimen), we are looking at the sheet surface. The compressive prestrain is horizontal. The tensile specimen is oriented perpendicular to the compression direction, and the split is in a plane perpendicular to the sheet surface and to the compressive prestrain. In Fig. 10(b) (cold rolling specimen), we are looking at the sheet thickness. The plane of the split is parallel to the sheet surface, i.e., perpendicular to the compressive prestrain (thickness strain).

Figure 11 shows the splitting behavior after cup drawing, IPC, BBS, and cold rolling, looking directly at the fracture surface.

After cup drawing to ε_{eff} = 0.57, a circumferential specimen shows only minor splitting (Fig. 11(a)). A radial specimen, on
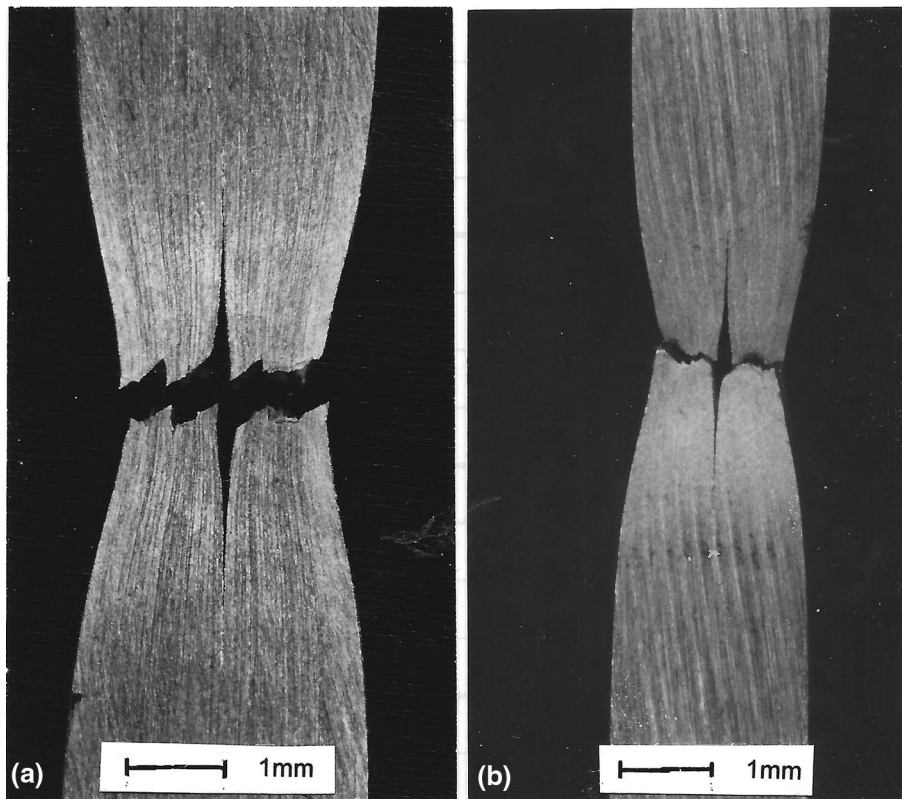
Fig. 10 Splits in tensile specimens after IPC to $\varepsilon_{\text{eff}} = 0.47$ (a) and cold rolling to $\varepsilon_{\text{eff}} = 0.6$ (b). The compressive prestrain is horizontal

the other hand, shows a major split in a radial plane of the cup flange, i.e., a plane perpendicular to the circumferential compressive prestrain (Fig. 11(b)).

After IPC to $\varepsilon_{\text{eff}} = 0.44$, a specimen parallel to the IPC direction (equivalent to circumferential direction in cup drawing) shows no major splitting (Fig. 11(c)). In contrast, a specimen perpendicular to the IPC direction (equivalent to radial direction in cup drawing) shows at least one major split in a plane perpendicular to the compressive prestrain (Fig. 11(d)). Finally, Fig. 11(e) and (f) shows specimens from cold rolling to $\varepsilon_{\text{eff}} = 0.68$ and BBS to $\varepsilon_{\text{eff}} = 0.72$, respectively, that both exhibit splits along planes parallel to the sheet surface, i.e., once again, perpendicular to the compressive prestrain.

4. Fracture Modes: SEM Examination of Fracture Surfaces and of Metallographic Cross-Sections of Charpy Specimens

4.1 Balanced Biaxial Stretching and Cold Rolling

4.1.1 Balanced Biaxial Stretching (BBS) Fracture Modes. A Charpy specimen containing two large splits (BBS to $\varepsilon_{\text{eff}} = 0.55$) is shown in Fig. 12(a). The two splits are shown in cross-sections in Fig. 12(b). Numerous smaller splits, approximately parallel to the sheet surface, can be seen in Fig. 12(c), which shows area R of the fracture surface. The large split in cross-section m–n, examined in detail by SEM using stereo-pairs, showed cleavage facets with clear river

markings and also broken up rare-earths inclusions, identified by EDX (Fig. 12(d)). Some of the splits in Fig. 12(c), examined by SEM, also showed evidence of cleavage fracture. In the slant portions of the fracture surface, dimpled rupture was the predominant fracture mode, but several larger, relatively smooth features were observed both directly on the fracture surface and in metallographic cross-sections. These features were identified as grain boundaries.

Similar features were observed in the slant regions (Fig. 13(a) and (b)), in another specimen after BBS ($\varepsilon_{\text{eff}} = 0.71$, specimen shown in Fig. 3d). In addition, small splits approximately parallel to the sheet surface, which appeared to exhibit grain boundary and cleavage fracture in stereo-examination, can be seen in Fig. 13(a) and (b). The grain boundary nature of the tip of one of these small splits is clearly evident in Fig. 13(d), which is an SEM picture of an etched metallographic cross-section perpendicular to the "plane" of the split.

4.1.2 Cold Rolling Fracture Modes. Figure 14 shows four pictures of a metallographic cross-section of a Charpy specimen from cold-rolled material ($\varepsilon_{\text{eff}} = 0.68$). The cross-section is perpendicular to the general direction of propagation of the fracture, which is predominantly slant but contains large splits, No. 1 and No. 2, approximately parallel to the sheet surface (Fig. 14(a)). The tips of these splits are seen at higher magnification in Fig. 14(b) and (c), respectively. A smaller split (No. 3), barely visible at the low magnification of Fig. 14(a), is shown in Fig. 14(d).

Higher-magnification SEM pictures (3KX to 6KX) of the extreme tips of the three splits are shown in Fig. 15. The tip of
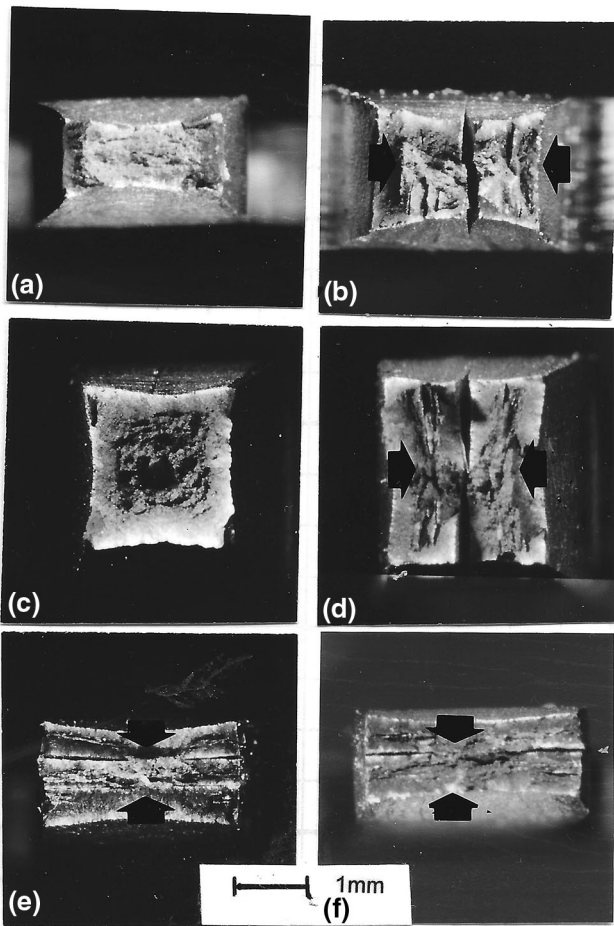
Fig. 11 Splits on the fracture surfaces of tensile specimens after cup drawing (a and b, $\varepsilon_{eff} = 0.57$), IPC (c and d, $\varepsilon_{eff} = 0.44$), cold rolling (e, $\varepsilon_{eff} = 0.68$), and BBS (f, $\varepsilon_{eff} = 0.72$). (a) Circumferential specimen. (b) Radial specimen. (c) Specimen parallel to compression direction. (d) Specimen perpendicular to compression direction. Sheet thickness direction is from top to bottom in all macrographs. Arrows indicate direction of compressive prestrain. Scale marker applies to all six specimens

split No. 1 (Fig. 15(a)) exhibits two non-connected branches. The branch that includes the very crack tip appears to be intergranular, judging from the different etching responses on the two sides of the branch. The other branch seems to be transgranular, judging from its straightness and from the same etching response on both sides. Figure 15(b) and (c) shows the middle and the tip of split No. 2, which is clearly intergranular. The fracture path along the tip of split No. 3 is also intergranular (Fig. 15(d)).

4.2 Type III Fracture Modes After Cup Drawing, IPC, and Uniaxial Tension

This low impact energy fracture, observed in all these three deformation modes above the critical prestrains in specimens parallel to the compressive prestrain, was predominantly macroscopically square, brittle in appearance, and the fracture plane was perpendicular to the compressive prestrain.

At higher magnification, however, a small zone of dimpled rupture was visible near the notch. The rest of the fracture (square region) exhibited a mixture of cleavage and intergranular fracture.

The size and morphology of the dimpled rupture zone varied with the impact energy level beyond the critical prestrain. For the lowest energy levels, a slant, very narrow fibrous zone was present all across the notch and there was no lateral contraction near the notch, indicating that the fibrous zone formed under plane strain. The brittle cleavage appeared to originate from regions slightly ahead of the fibrous zone (approximately 300 μm), based on the directions of the chevrons and of the river markings on the cleavage facets. For the highest energy levels, there was a larger zone of slant fibrous fracture near the notch and a significant amount of lateral contraction (Fig. 16(a)). In addition, a triangular zone of square fibrous fracture, exhibiting clear tension dimples, was adjacent to the slant fracture (Fig. 16(a) and (b)). Brittle cleavage started at the tip of the triangular zone (Fig. 16(b)).

Throughout the brittle zone, both cleavage and intergranular fracture occurred. This was established by extensive examination of SEM stereo-pairs and by metallographic examination of nickel-plated cross-sections of the fracture surface. Figure 16(c) and (d) shows typical brittle zone regions containing several cleavage facets with river markings and instances of intergranular fracture.

4.3 Type IV(A) Fracture Modes (Cup Drawing, Radial Specimens)

The macroscopic path of this fracture is described in Sect. 3.2.2. The fracture started as a fibrous fracture propagating in the circumferential direction (direction imparted by the loading of the Charpy specimen), but then the fracture continued as a square fracture in a roughly perpendicular direction, i.e., in a "plane" roughly perpendicular to the compressive prestrain. This change in direction was caused by the strong anisotropy resulting from this particular mode of cold work. The fibrous fracture consisted predominantly of dimples, and the square fracture exhibited radiating chevrons (consisting of shear dimples) separated by planes of brittle fracture modes, i.e., cleavage and intergranular fracture. The transition from the dimpled rupture region to the square brittle fracture is shown in Fig. 17(a), where a large split can be seen in the dimpled region. The plane of this split is roughly parallel to the beginning of the main square brittle fracture. Although this particular split did not propagate to complete fracture, its presence reflects the tendency for fracture to occur preferentially in planes perpendicular to the compressive prestrain. Figure 17(b) and (c) shows the presence of cleavage on the surface of the split.

4.4 Type IV(C) Fracture Modes (IPC, Specimens Perpendicular to the IPC Direction)

The macroscopic features of this fracture type are described in Sect. 3.3.2 and illustrated in Fig. 8. SEM examination of the fracture beyond the narrow fibrous zone near the notch showed a mostly square, brittle fracture, consisting of cleavage and intergranular fracture, propagating on several parallel planes connected by walls of shear dimples (Fig. 18). The square fracture followed a curved path that deviated strongly from the expected path in a typical Charpy specimen. Examination of a metallographic cross-section parallel to the sheet surface in a broken Charpy specimen revealed that the fracture path exhibited a segmented appearance with some portions roughly perpendicular to the compression direction.
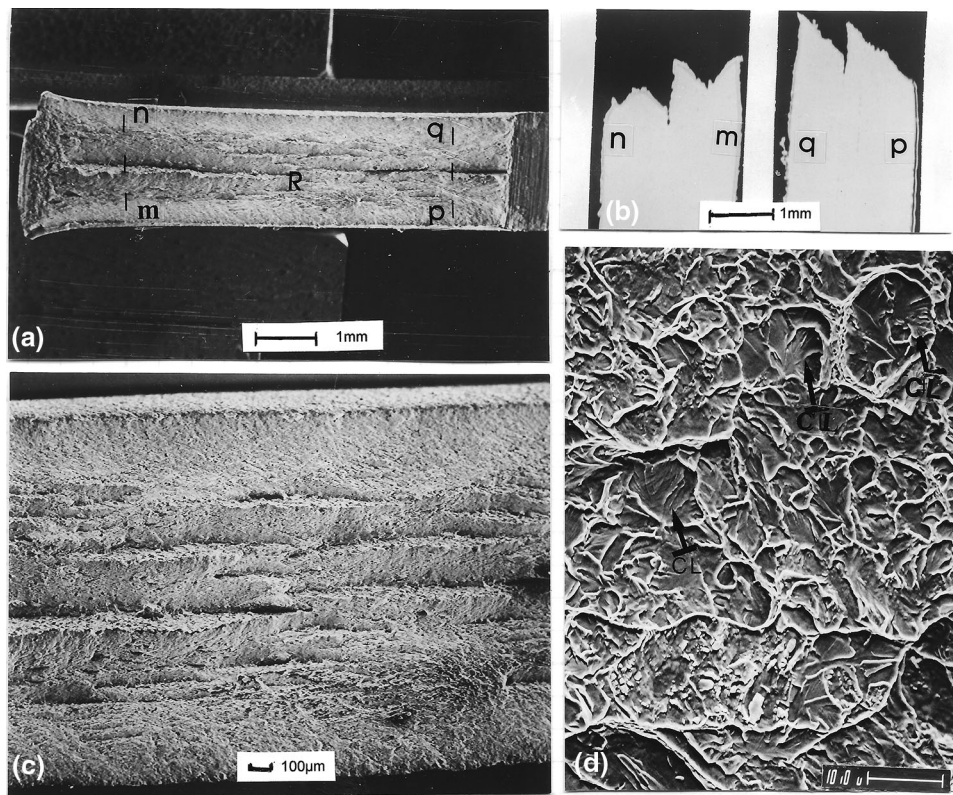
Fig. 12 Brittle splits parallel to the sheet surface in a Charpy specimen after BBS to ε_{eff} = 0.55. (a) Overall fracture surface. (b) Metallographic cross-sections through m–n and p–q showing two large mid-thickness splits. (c) Splits in area R of the fracture surface. (d) SEM micrograph of the large split in section m–n showing cleavage facets (CL) with river markings

5. Effect of Prestraining on Crystallographic Textures, Inclusions, Carbides, and Grain Shape

5.1 Textures

As indicated in Sect. 1.1, previous investigators have pointed out the possible role of crystallographic texture in producing anisotropic embrittlement after cold work.

In this investigation, crystallographic textures were determined after in-plane compression, balanced biaxial stretching, and cold rolling. First, standard X-ray pole figures were obtained to establish the nature of the textures, and then diffraction peak intensities of low index planes normal to the compressive prestrain were measured.

After in-plane compression, the texture was found to be a double fiber texture, <111> + <100>, with the compression direction as the fiber axis. After BBS, the texture was the same double fiber texture, but with the fiber axis normal to the sheet surface. After cold rolling, the main texture is a partial fiber texture, (001) $[\bar{1}10]$ to (111) $[\bar{1}10]$ in which the fiber axis is parallel to the cold rolling direction.

The integrated intensities of 8 diffraction peaks, (110), (200), (211), (310), (222), (321), (420), and (332) were measured for several prestrain levels for the three deformation modes. These measurements were made in a plane parallel to the sheet surface at the quarter thickness position after BBS and cold rolling and in a plane normal to the compression direction after IPC, using composite samples. The relative peak inten-

sities, I_{hkl} (textured sample)/I_{hkl} (non textured), expressed in (times random) units, are shown in Fig. 19. The (200) and (222) components, and to a lesser extent the (332) component, increase during deformation at the expense of all the others. However, the increase is significantly less after cold rolling than after BBS or IPC.

5.2 Deformation Damage at Inclusions and Carbides

Metallographic cross-sections of the deformed materials were examined by SEM. The presence of cracks and voids near non-metallic inclusions and carbides was investigated.

5.2.1 Inclusions. In the hot-rolled condition, many of the inclusions (rare-earth oxy-sulfides) were intact, i.e., without cracks. However, some inclusions exhibited internal cracks more or less normal to the hot rolling direction. In addition, interfacial voids were sometimes observed in alignments of inclusions, suggesting relatively low matrix/inclusion interface strength.

After cold rolling, inclusions generally exhibited more extensive internal cracking (Fig. 20(a)). The internal cracks were roughly normal to the cold rolling direction. In addition, voids at the inclusion/matrix interfaces were often present in alignments of inclusions parallel to the cold rolling direction. Finally, a few microcracks, roughly normal to the sheet thickness direction (compressive prestrain direction), were present at the "corners" of some of the angular, blocky inclusions, sometimes along a grain boundary, sometimes in the matrix (Fig. 20(b) and (c)).
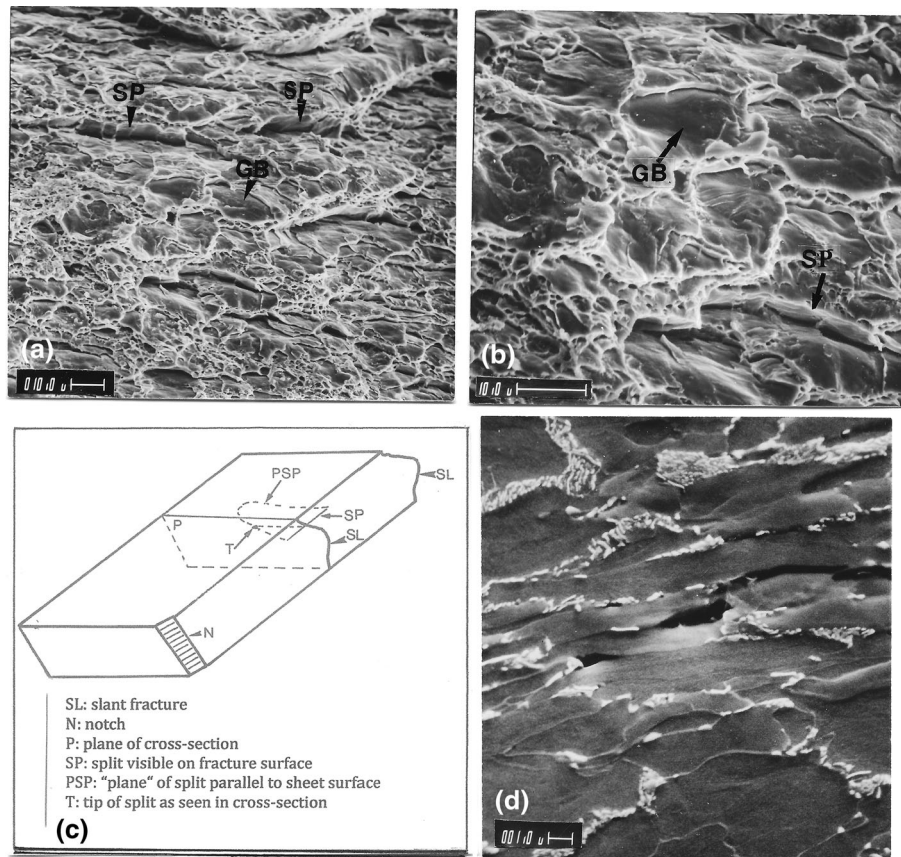
Fig. 13 (a, b) SEM micrographs of the slant region in the Charpy specimen in Fig. 3d (BBS, $\varepsilon_{eff} = 0.71$) showing dimples, grain boundary fracture (GB) and small splits (SP) parallel to the sheet surface. (c) Schematic describing the orientation and location of the SEM micrograph in (d) showing the intergranular tip of brittle split

After BBS, two types of inclusion damage were observed: widely open internal cracks perpendicular to the hot rolling direction and large voids surrounding the inclusions. In cross-sections parallel to the sheet surface, these voids appeared circular, as expected from the symmetry of the applied stress.

After cup drawing, the cracks and microcracks had the same orientation relationship to the compressive prestrain as after cold rolling. Figure 20(d) shows inclusions in the flange of a cup where $\varepsilon_{eff} = 0.55$. The plane of the pictures is parallel to the sheet surface, and the circumferential direction is from top to bottom. Microcracks roughly perpendicular to the circumferential direction and extending into the matrix or along a grain boundary can be seen at the "corners" of some inclusions.

After IPC, a few inclusions exhibited internal cracking perpendicular to HRD. Others showed extensive internal cracks roughly parallel to the compression direction.

5.2.2 Carbides. Microvoids were seen at carbide particles in as-deformed BBS material, especially after high prestrains. Many microvoids were present for $\varepsilon_{eff} = 0.71$, but fewer were seen for $\varepsilon_{eff} = 0.44$. The microvoids were almost always located on grain boundaries (Fig. 21). No microvoids were observed after cold rolling or IPC after the largest prestrains. This indicates that a tensile stress state is required to produce these microvoids. This is further confirmed by the presence of microvoids at carbide particles (Fig. 21(e)), just below the slant fracture surface in the Charpy specimen shown in Fig. 14 (cold rolling, $\varepsilon_{eff} = 0.68$) but the absence of microvoids further away

from the fracture surface, i.e., in the as-cold-rolled material not affected by the fracture process. This observation is consistent with the fact that a triaxial tensile stress state is known to exist ahead of the propagating fracture in the Charpy specimen.

5.3 Grain Shape

During plastic deformation, the grains undergo the same shape change, on average, as the macroscopic shape change of the workpiece. For example, grains become flattened (reduced in thickness) and enlarged equibiaxially during BBS and flattened plus elongated with no width change during cold rolling (plane strain deformation). During cup drawing, there is a compressive strain in the circumferential direction of the flange and a tensile strain in the radial direction. Therefore, the grains become elongated in the radial direction and reduced in width in the circumferential direction. The grain thickness usually increases because, typically, the hold-down pressure is insufficient to prevent thickening of the flange. The changes in grain shape during IPC are similar to those during cup drawing. The grain shape changes after IPC to $\varepsilon_{eff} = 0.46$ and after cup drawing to $\varepsilon_{eff} = 0.62$ are illustrated in Fig. 22. After IPC to $\varepsilon_{eff} = 0.46$, the longitudinal strain, compressive strain, and thickness strain were, respectively, $\varepsilon_l = 0.25$, $\varepsilon_c = -0.46$, and $\varepsilon_{th} = 0.21$. Therefore, one would expect to observe, on average, a 28.4% grain elongation [exp(0.25) = 1.284] and a 37% width contraction [exp(-0.46) = 0.63]. These numbers are compat-
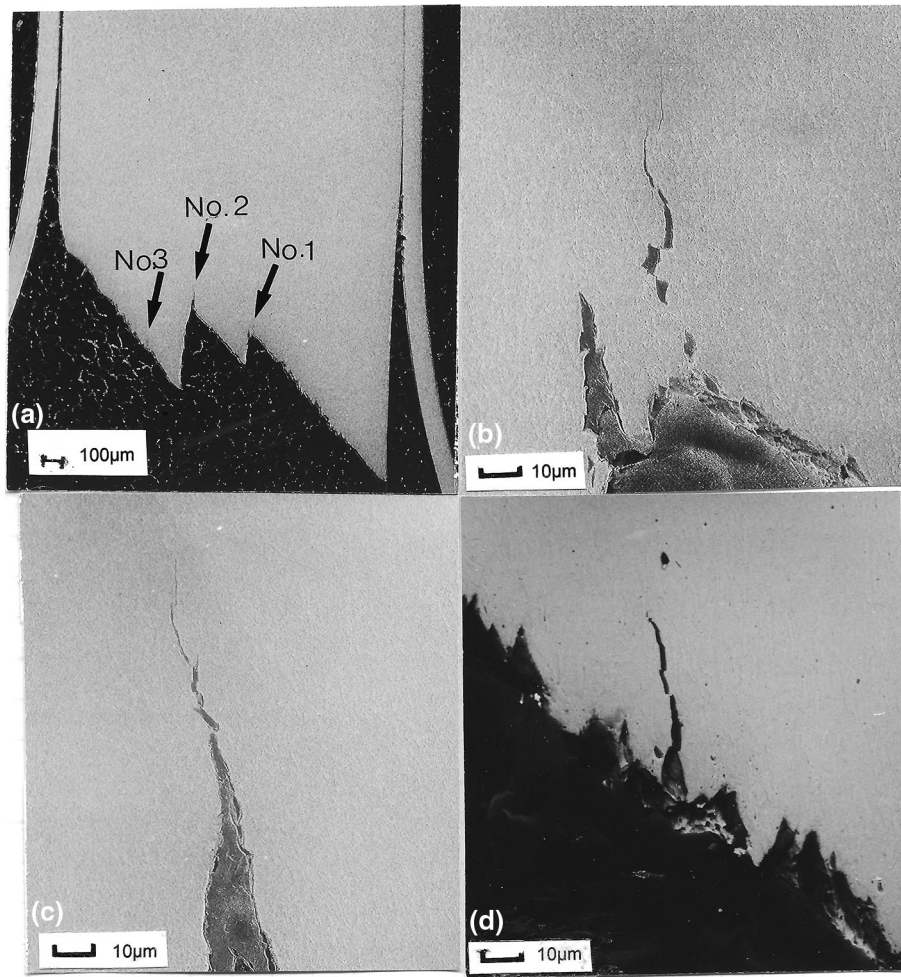
Fig. 14 Metallographic cross-section perpendicular to the general direction of fracture propagation in Charpy specimen after cold rolling ⊥ HRD to $\varepsilon_{eff} = 0.68$. (a) Full thickness cross-section. (b, c, d) Higher-magnification views (original 600 X) of splits 1,2, and 3, respectively

ible with the micrographs in Fig. 22(a) and (b). After cup drawing to $\varepsilon_{eff} = 0.62$, the three principal strains were $\varepsilon_l = 0.395$, $\varepsilon_c = -0.61$, and $\varepsilon_{th} = 0.215$. These logarithmic strains correspond to average grain elongation and width contraction values of 48% [exp(0.395) = 1.48] and 46% [exp(− 0.61) = 0.54], respectively. These results are also in qualitative agreement with the microstructures observed in Fig. 22(a) and (c).

6. Discussion

6.1 General

All the above results clearly indicate that a compressive prestrain of sufficient magnitude, produced by cold forming, can lead to post-forming anisotropic embrittlement along planes that are roughly perpendicular to the compressive prestrain. The stress state under which the compressive prestrain is produced does not appear to influence this result. For example, brittle splits parallel to the sheet surface can occur after deformation in biaxial stretching, a purely tensile stress deformation mode, as well as after cold rolling, a purely compressive stress mode. The details of the fracture behavior are determined by the response of the anisotropic microstructure to the prevailing stress system during testing.

6.2 Requirements for Completely Brittle Behavior

Level of prestrain, orientation of the tensile stress system during testing (or in service) relative to the compressive prestrain, and presence or absence of stress triaxiality all influence the overall energy absorption during fracture and the macroscopic fracture appearance.

Low-energy fracture associated with a square brittle fracture occurs when the following three conditions exist:

1. the compressive prestrain is larger than a critical value
2. the primary tensile testing stress is in the direction of the compressive prestrain
3. the operating stress system is triaxial

Such a situation occurs after both cup drawing and in-plane compression in Charpy specimens that are parallel to the compressive prestrain. As a result, the plot of specific impact energy versus prestrain exhibits an abrupt drop at a critical prestrain and the fracture is square and brittle. The critical prestrain depends on the specimen thickness. It decreases with increasing thickness as indicated in Sects. 3.2.1 and 3.3.
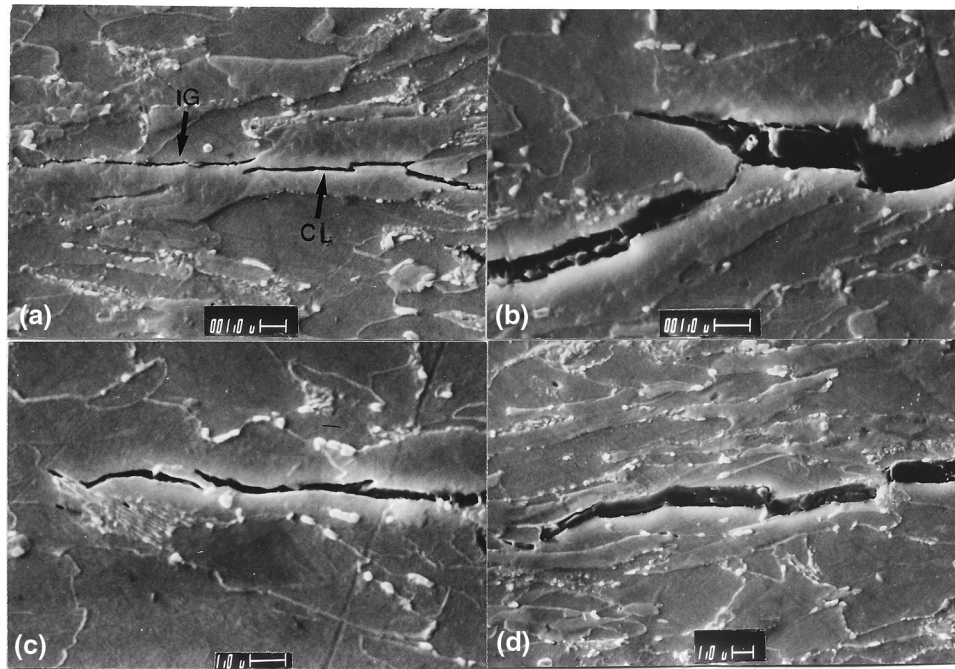
Fig. 15 SEM micrographs of etched metallographic cross-sections of splits shown in Fig. 14. (a) Tip of split No. 1 showing cleavage and intergranular (IG) fracture. (b) Middle of split No. 2 showing IG fracture. (c) Tip of split No. 2 showing IG fracture). (d) Tip of split No. 3 (IG fracture). The general direction of crack propagation is from right to left

6.3 Testing Stress Perpendicular to Compressive Prestrain

In contrast, when the primary tensile testing stress is perpendicular to the compressive prestrain (Charpy specimens perpendicular to the prestrain direction), even when triaxiality is present and the prestrain is above the critical value, the results are more complicated, in terms of both fracture energy and macroscopic fracture appearance. In particular, in this orientation, the fracture behavior is different after cup drawing and after in-plane compression. After cup drawing, the fracture energy remains high beyond the critical prestrain (Fig. 4), but after IPC the fracture energy drops to low levels (Fig. 7). This difference in energy behavior is consistent with the difference in fracture appearance. After cup drawing, the fractures exhibit first a slant fracture region (high energy) then a square fracture region, or vice versa (Fig. 6). The regions of square fracture follow approximately planes that are perpendicular to the prior compressive strain (direction of easy crack propagation) and are initiated under the action of the "forward" component of the triaxial stress state ahead of the propagating crack. After IPC, the fractures appear to be predominantly square but follow a more or less curved path (Fig. 8). The fracture, examined at higher magnification, consists of segments of square fracture perpendicular to the compressive prestrain joined by shorter segments of shear fracture, both of which combine to produce the observed curved path.

6.4 Role of Stress Triaxiality and Specimen Thickness

6.4.1 Stress Triaxiality, Specimen Thickness, and Critical Prestrain. As indicated in Sect. 3.2.1(*footnote*), the critical prestrains for brittle fracture after cup drawing were significantly lower in full thickness circumferential Charpy specimens than in prethinned specimens. Also, as described in

Sect. 3.3.1 the critical prestrains after IPC (thick specimens) were lower than after cup drawing of prethinned blanks (thin specimens). Thus, thick Charpy specimens can be said to be more prone to embrittlement than thin specimens. This result is attributed to the difference in triaxial stress state ahead of the notch, i.e., the transverse stress is relatively larger in thick specimens than in thin specimens, thus producing a stress state closer to plane strain, which favors brittle fracture. Therefore, a higher degree of triaxiality results in lower critical prestrains.

6.4.2 Comparison Between Charpy and Tensile Specimens Behaviors. The important role of the triaxial stress state during post-forming testing in promoting brittle fracture is made clear by comparing the behavior of Charpy and tensile specimens both parallel to the compressive prestrain after cup drawing and IPC. For similar levels of prestrain (above the critical prestrains), brittle fracture occurs in the Charpy specimens (Fig. 4 and 7), but not in the tensile specimens (Fig. 11(a) and (c)).

In both cases, the primary applied stress has the same orientation with respect to the compressive prestrain, i.e., it is parallel to that prestrain. However, a triaxial stress state is present ahead of the notch and of the fracture front in the Charpy specimens, whereas this is not the case in the tensile specimens, at least until the neck develops.

Furthermore, when the neck finally develops, the triaxial stress state that appears at that point is no longer acting on the as-prestrained microstructure because the microstructural changes produced by the compressive prestrain (grain shape changes and crystallographic texture) have been "undone" or "reversed" by the tensile strain during the beginning of the tensile test, thus eliminating the possibility of brittle fracture.

In the "radial" tensile specimens after cup drawing and IPC, the situation is different. The deformation during tensile testing produces an additional compressive strain, in the same direction
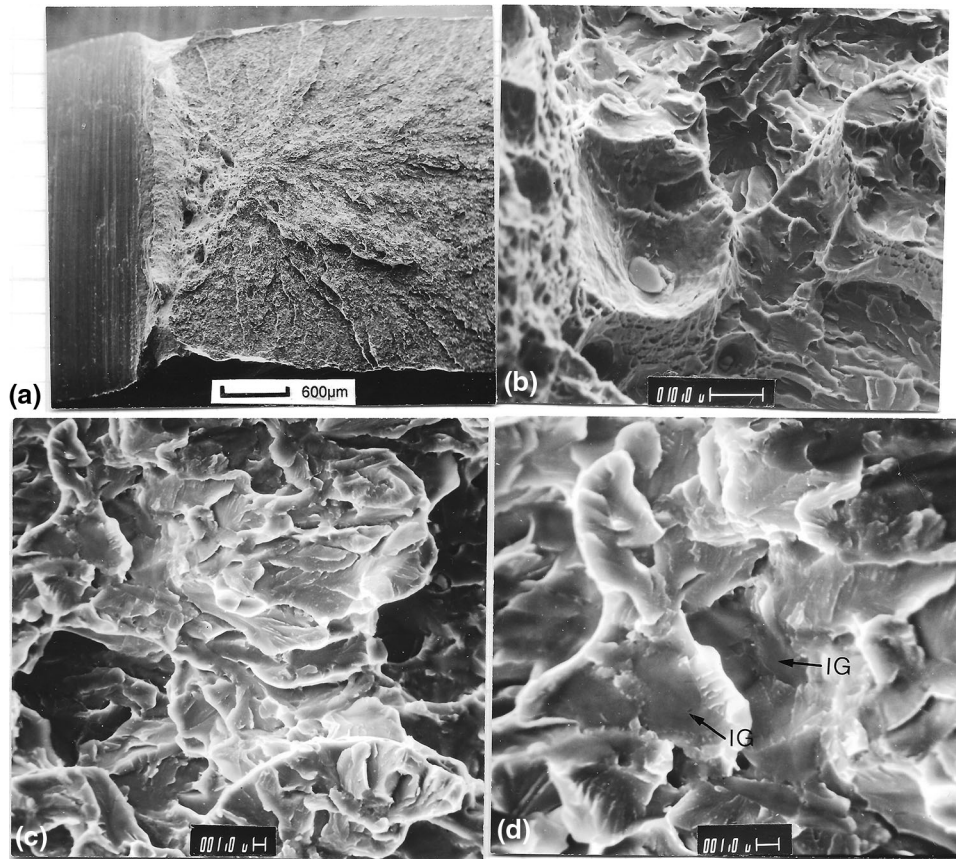
Fig. 16 Typical SEM micrographs in type III brittle fracture in Charpy specimens parallel to the compressive prestrain after cup drawing, IPC, or uniaxial tension. (a) Full thickness macroview showing both the slant and the square fibrous zones near the notch after IPC to ε_{eff} = 0.34. (b) Beginning of cleavage fracture near a large dimple (containing a rare-earth inclusion) located on the edge of the slant fibrous fracture after cup drawing to ε_{eff} = 0.62. (c) Numerous cleavage facets with river markings and a few examples of intergranular fracture (cup drawing to ε_{eff} = 0.62). (d) Higher-magnification view of intergranular regions in (c). General direction of fracture propagation in all micrographs is from left to right

as the compressive prestrain, due to the lateral contraction of the specimen both before and after necking. In the end, splitting occurs along planes perpendicular to the total compressive prestrain under the primary action of the transverse neck stress that is parallel to that prestrain. The large brittle splits in the tensile specimens illustrated in Fig. 11(b) and (d) can thus be qualitatively understood by the presence of the triaxial stress state that develops in the neck of the specimens. In the tensile specimens from BBS and cold rolling (Fig. 11(e) and (f)), the deformation during testing also produces an additional compressive strain (in the sheet thickness direction) and, again, splitting occurs on planes that are perpendicular to the compressive prestrain, i.e., parallel to the sheet surface.

6.4.3 Comparison Between Charpy Specimens After Cup Drawing and IPC. As described earlier, the fracture behavior is similar after cup drawing and IPC for Charpy specimens parallel to the compressive prestrain (type III fracture beyond the critical prestrain). However, the difference in fracture behavior between cup drawing and IPC for Charpy specimens perpendicular to the compressive prestrain needs to be discussed. Although the difference in impact energy behavior for this orientation beyond the critical prestrains is consistent with the fact that type IV(A) fractures after cup drawing exhibit some regions of slant fracture (high energy

absorption), whereas type IV(C) fractures after IPC are all largely square and brittle (low energy absorption), the question remains: "why do we observe these two types of fracture"? One obvious difference between the two groups of specimens is their thickness (typically 3.3 mm after IPC versus 2 mm after cup drawing). To explore whether the difference in thickness may be responsible for the difference in fracture type and energy, Charpy specimens from IPC material of the same prestrain level as the cup drawn specimens were reduced in thickness by surface grinding to match the thickness after cup drawing. It was observed that the fracture changed from type IV(C) to type IV(A) as a result and the specific impact energy increased. Thus, in this specimen orientation thickness also affects the fracture behavior. The change in fracture appearance and the increase in specific impact energy with decreasing thickness is understandable because the constraint and the degree of triaxiality at the notch tip and fracture front is lessened by the decrease in thickness.

6.4.4 Conclusion on Thickness Effect. Overall, therefore, the thickness effect is important to keep in mind, particularly for performance in service, since it indicates that, all other things being equal, greater thicknesses will lead to easier embrittlement.
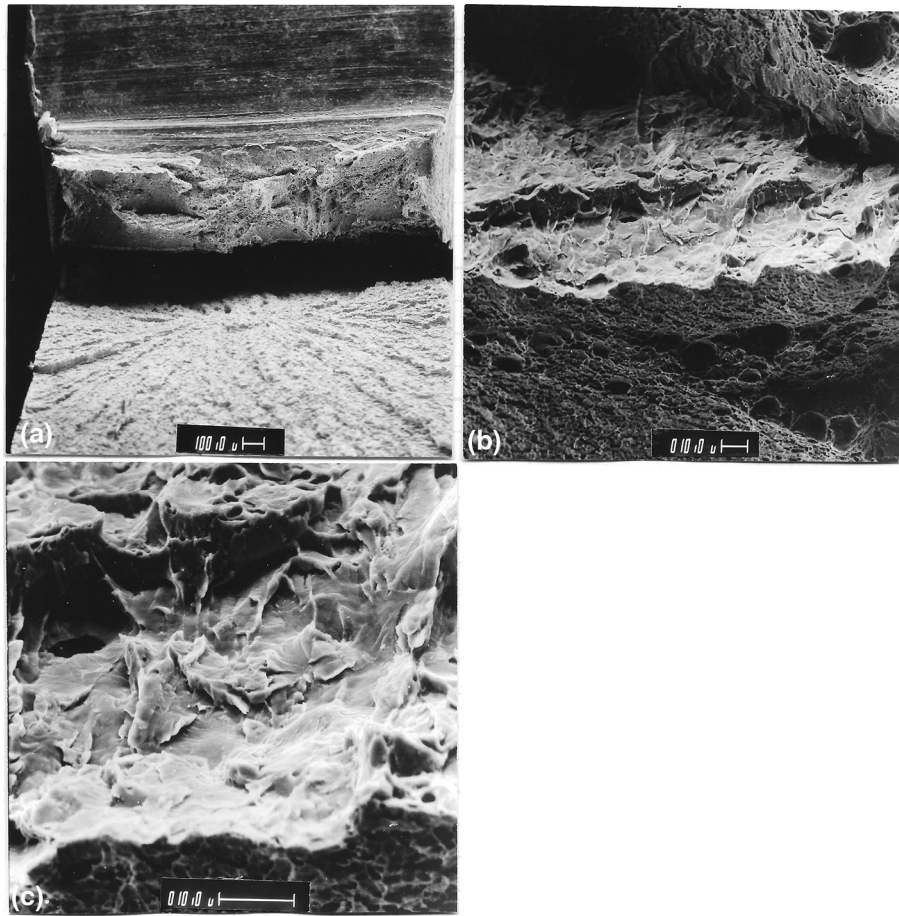
Fig. 17 SEM micrographs showing type IV(A) fracture appearance in radial Charpy specimen after cup drawing *to* ε_{eff} = 0.6. (a) Fracture appearance near the notch showing large brittle split in zone of fibrous fracture. (b, c) Cleavage fracture on surface of large split

6.5 Microstructural Mechanisms

Whereas the effect of the compressive prestrain on anisotropic post-forming embrittlement is well supported by the data, the exact nature of the microstructural mechanisms responsible for the embrittlement is not so clear.

Three main factors appear to play a role: the crystallographic texture produced by the prestrain, the microstructural damage at non-metallic inclusions and carbides, and the elongated grain shape. These three factors interact in a complicated manner in the initiation and propagation of the brittle fracture, which consists of both cleavage and intergranular modes.

It is conceivable that the inclusion/matrix interfacial voids along lines of inclusions together with the associated matrix microcracks could be locations where brittle fracture initiates either by cleavage or intergranularly. In contrast, whether the small voids present near grain boundary carbides after BBS could initiate fracture is unclear. However, Fig. 13(d) suggests that the carbides play a role in the propagation of the intergranular fracture. It is also likely that intergranular fracture is made easier by the grain elongation resulting from the prestrain. As for the crystallographic texture, it probably contributes to embrittlement by the cleavage mechanism. The

enhancement of the cleavage plane component (200) after BBS and IPC is consistent with the presence of cleavage fracture on planes perpendicular to the compressive prestrain. The increase in that component is much less after cold rolling, and this may account for the many instances of intergranular fracture, rather than cleavage, observed in Fig. 15. However, whether the amount of cleavage fracture is overall quantitatively less, relative to intergranular fracture, on all the brittle splits after cold rolling than after BBS is uncertain since no attempt was made to answer this question.

7. Summary and Conclusions

1. The post-forming fracture behavior of the Van-80 HSLA steel sheet investigated depends in complex ways on the mode and amount of prior deformation and on the orientation of the stress system during testing (or in service) with respect to the principal axes of the prior deformation.
2. The post-forming fracture behavior is anisotropic. Specifically, brittle fracture can occur preferentially along
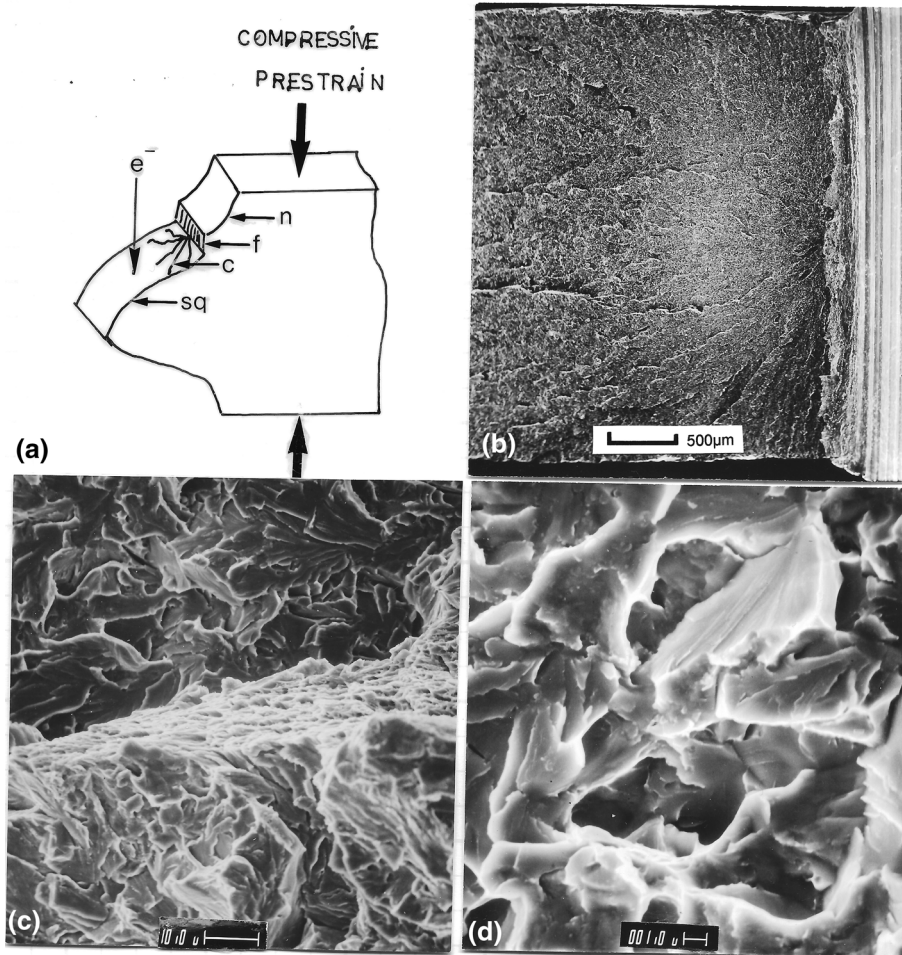
Fig. 18 Type IV (C) fracture after deformation by IPC to large prestrain (ε_{eff} = 0.47). Charpy specimen perpendicular to the compressive prestrain. (a) Sketch showing orientation of specimen in the SEM. (b) Overall appearance showing small fibrous region near notch and radiating chevrons. (c) Wall of shear dimples between plateaus of brittle fracture. (d) Typical cleavage and intergranular fracture in square brittle zone between walls of shear dimples

planes that are perpendicular to the prior compressive strain, regardless of the mode of deformation and stress state producing this compressive prestrain. Both cleavage and intergranular fracture are present along those planes.

3. This anisotropy can lead to different macroscopic forms of fracture, such as square brittle fractures after drawing and splitting fractures after biaxial stretching, depending on the orientation of the primary testing stress relative to the prior compressive strain.

4. A sufficient level of prestrain is needed for brittle fracture to occur.

5. This level of prestrain depends on stress triaxiality. This explains why thick sheets are more prone to embrittlement than thin sheets.

6. Grain shape and crystallographic texture changes produced by the various types of prestrains as well as cracks and voids at non-metallic inclusions and carbides were examined. Although these changes are consistent with the observed embrittlement, the detailed microstructural mechanisms causing the fracture need to be further investigated.

7. To avoid brittle fractures or splitting fractures in service, it is desirable, if possible, to minimize the level of compressive prestrain, minimize sheet thickness, avoid notches at sheared edges, and avoid impact loading.
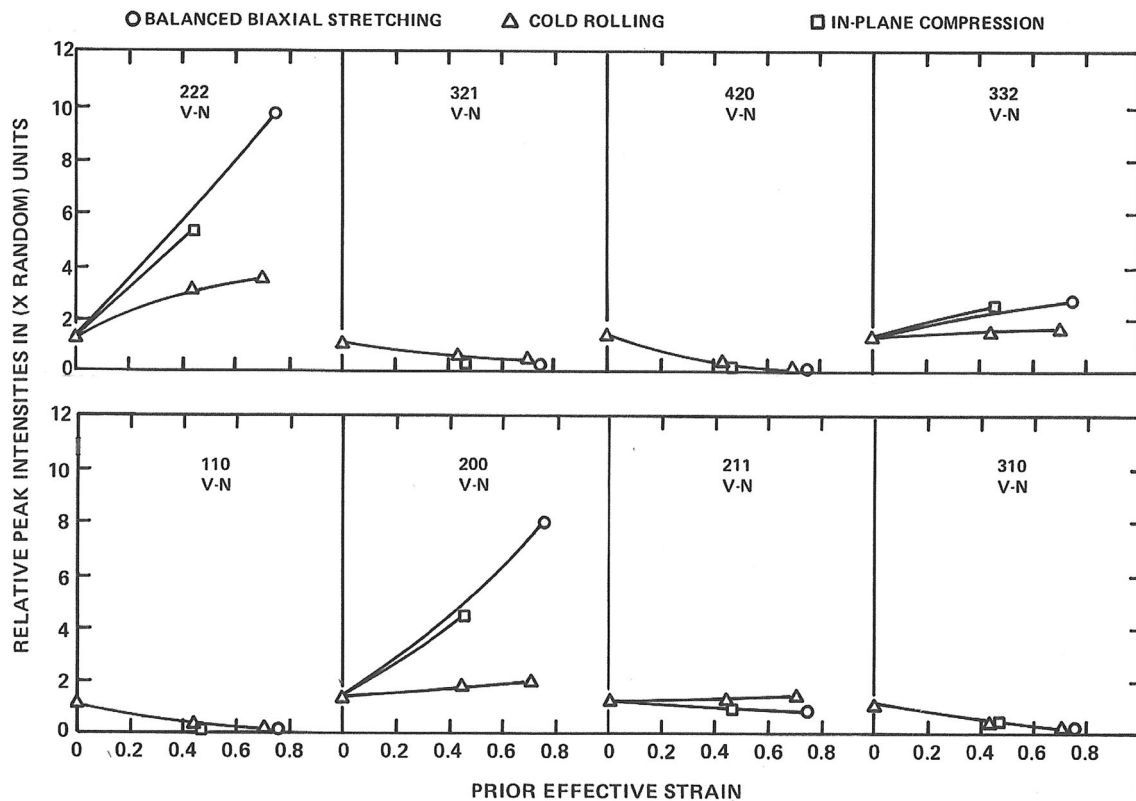
Fig. 19 Crystallographic texture components, for the vanadium-nitrogen steel (V-N) investigated, after deformation by BBS, cold rolling, and IPC
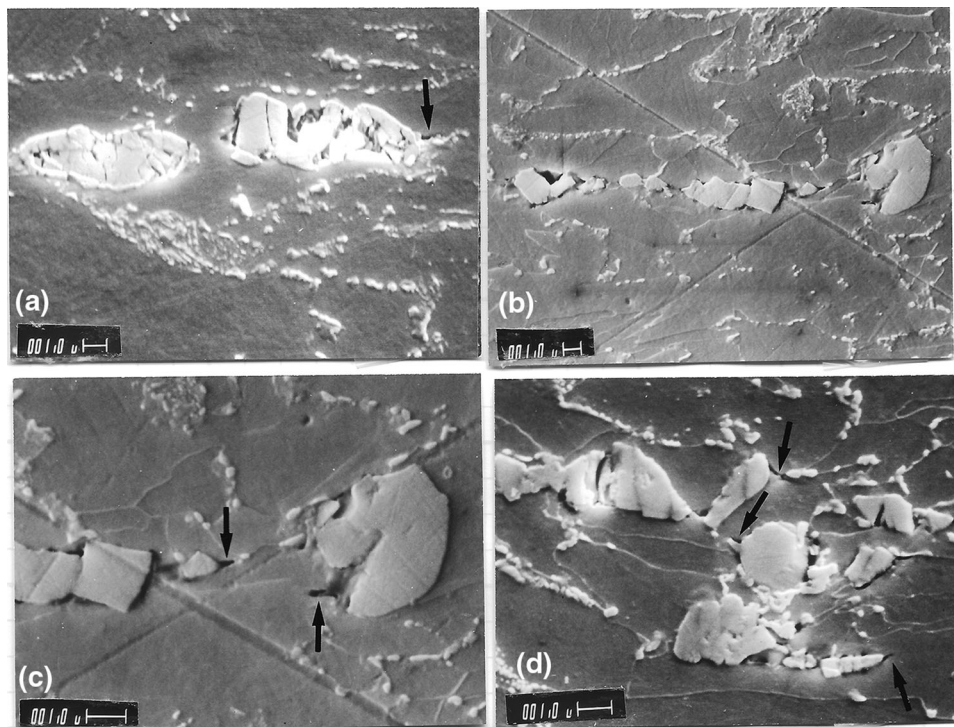

Fig. 20 Examples of cracks and microcracks produced inside and near inclusions by cold rolling and cup drawing. (a) Large internal cracks after cold rolling ⊥ HRD to $\varepsilon_{eff} = 0.68$. Cold rolling direction is horizontal. Sheet thickness direction is top to bottom. (b, c) Cracks and microcracks in matrix and on grain boundary after cold rolling⊥ HRD to $\varepsilon_{eff} = 0.68$. HRD is horizontal and cold rolling direction in into sheet of paper. (d) Microcracks in matrix and on grain boundary after cup drawing to $\varepsilon_{eff} = 0.55$. Plane of the micrograph is parallel to the cup flange surface. Circumferential direction is from top to bottom

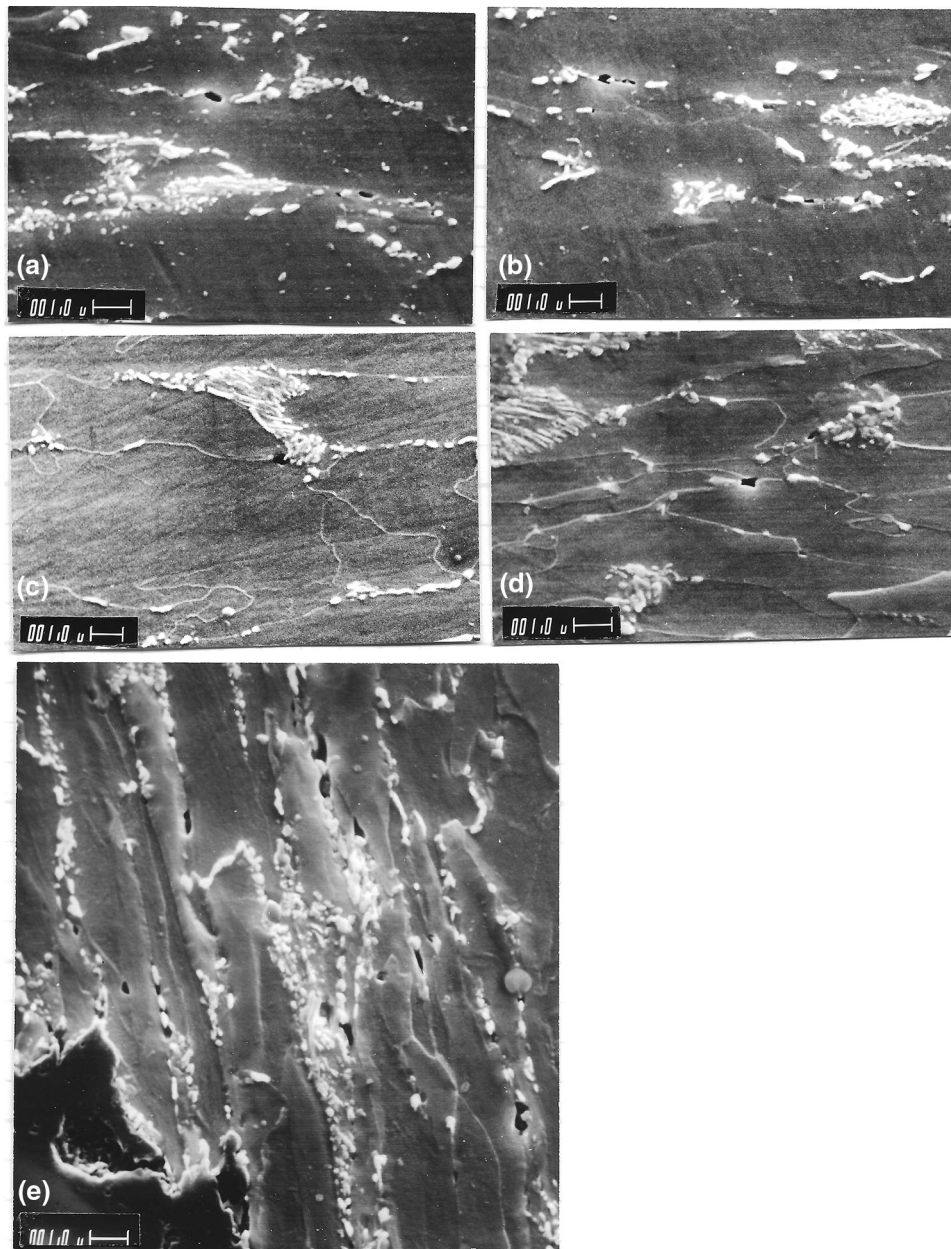**Fig. 21** Microvoids at carbides on grain boundaries. (a–d) After BBS to $\varepsilon_{eff} = 0.71$. Thickness direction is from top to bottom. (e) Cross-section near slant fracture of Charpy specimen after cold rolling to $\varepsilon_{eff} = 0.68$. Sheet thickness direction is horizontal. Small portion of fracture surface is seen in lower left corner
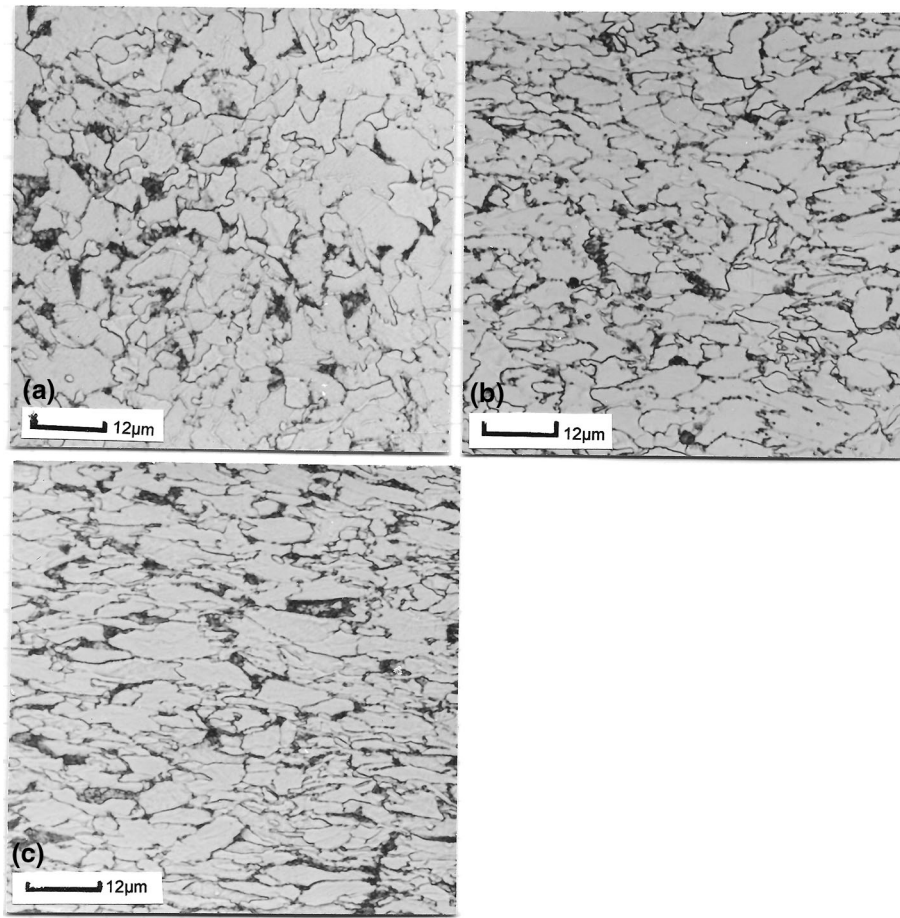
Fig. 22 Optical micrographs, parallel to sheet surface, showing grain elongation after IPC and cup drawing (original magnification 1000 X). (a) As-received. (b) IPC to $\varepsilon_{\text{eff}} = 0.46$. Compression direction is from top to bottom. (c) Cup drawing to $\varepsilon_{\text{eff}} = 0.62$. Flange circumferential direction is from top to bottom. Hot rolling direction is from top to bottom in all cases

References

1. F. Garofalo and J.R. Low, Jr., The Effect of Prestraining in Simple Tension and Biaxial Tension on Flow and Fracture Behavior of a Low Carbon Deep Drawing Steel Sheet, *J. Mech. Phys. Solids*, 1955, **3**, p 275–294
2. K. Yoshida et al., Anisotropic Behavior of Prestrained Sheet Steels and Subsequent Formability, *Tetsu to Hagane*, 1969, **55**, p 26–47
3. K. Miyauchi, Prestrain Induced Behaviors of Mechanical Properties and Press Formabilities in Sheet Metals, *Paper Presented at the 1976 Colloquium of the International Deep Drawing Research Group, Ann Arbor, MI*
4. A.K. Ghosh and W.A. Backofen, Strain Hardening and Instability in Biaxially Stretched Sheets, *Metall. Trans.*, 1973, **4**, p 112–123
5. A.K. Ghosh and J.V. Laukonis, The Influence of Loading Path Variations on Flow Stability in Steel Sheets, *Proceedings of the Second International Conference on Mechanical Behavior of Materials, ASM*, 1976, p 278-282
6. P.L. Charpentier and H.R. Piehler, Properties of Formed Parts: Flow and Fracture Behavior after Cold Forming in HSLA Steel Sheets, *Mém. Sci. Rev. Métall.*, 1980, **77**(3), p 281–292
7. P.L. Charpentier and H.R. Piehler, In-Plane Compression: A New Laboratory Forming Technique to Study the Effect of Large Drawing Deformations in Sheets on Their Subsequent Mechanical Behavior, *J. Test. Eval. JTEVA*, 1983, **11**(1), p 46–55
8. P.L. Charpentier and H.R. Piehler, Yielding Anisotropy from the Bauschinger Effect and Crystallographic Texture in Drawn HSLA Steel Sheet, *Metall. Trans.*, 1984, **15A**, p 1699–1710
9. M. Konishi, M. Nishida, and N. Ohashi, Brittle Fracture of Steel Sheets and Press Forming, *Presented at the 8th Biennial Congress of the International Deep Drawing Research Group, Gothenburg, Sweden*, 1974
10. K. Matsudo, K. Osawa, M. Yoshida, and M. Sakoh, Relationship Between the Brittleness of Steel Sheets Induced by Deep Drawing and Material Characteristics of Sheet Materials, *Nippon Kokan Technical Report-Overseas*, April 1977, p 15–24
11. D.C. Drucker, C. Mylonas, and G. Lianis, Exhaustion of Ductility of E-Steel in Tension Following Compressive Prestrain, *Weld. J.*, 1960, **39**(3, Research Supplement), p 117s–120s
12. C. Mylonas, S. Kobayashi, and A.E. Armenakas, Exhaustion of Ductility under Notch Constraint Following Uniform Prestraining, *Trans. AIME*, 1969, **245**(5), p 919–927
13. C. Mylonas, The Mechanics of Brittle Fracture, *in Proceedings of the 11th International Congress of Applied Mechanics, Munich*, 1964, ed. by H. Gorther (Springer, Berlin, 1966), p 652–660

14. W.L. Brenneman and H.C. Rogers, Effect of Prestrain on Tensile Ductility of Armco Iron, *J. Metals JOM*, 1975, **27**(12), p A38

15. W.L. Brenneman and H.C. Rogers, The Role of Texture on Prestrain Embrittlement of Armco Iron, in *Fourth International Conference on Fracture, June 1977, University of Waterloo, Canada,* 1978, p 123–129

16. C.A. Garcia, M. Hua, A.J. DeArdo, and H.R. Piehler, Forming Strain Path and Cold Work Embrittlement in Sheet Steels, *SAE Technical Paper 2002-01-0043,* 2002, p 1–8

17. P.L. Charpentier, Post-forming Monotonic and Cyclic Behavior of a HSLA Steel Sheet after Large Deformations by In-Plane Compression, *Int. J. Fatigue*, 2015, **79**, p 55–64

18. H. Takechi, Metallurgical Aspects of Interstitial-Free Sheet Steel from Industrial Viewpoints, *ISIJ*, 1994, **34**(1), p 1–8

19. S.P. Bhat, B. Yan, J.S. Chintamani, and T.A. Bloom, Secondary Work Embrittlement of Stabilized Steels: Test Methods and Applications, *Iron Steelmak.*, 1995, **17**(9), p 33–42

20. D. Li, G. Hessling, and W. Bleck, The Secondary Work Embrittlement in Sheet Steels, *Steel Res.*, 1999, **70**(4–5), p p154–p161

21. J.S. Rege, M. Hua, G.I. Garcia, and A.J. DeArdo, The Segregation Behavior of Phosphorous in Ti and Ti + Nb Stabilized Interstitial-Free Steels, *ISIJ Int.*, 2000, **40**(2), p 191–199

22. K.P. Boyle, Cold Work Embrittlement of Interstitial-Free Sheet Steel, Ph.D. thesis, McMaster University, 2001

23. F. Kitano, T. Urabe, T. Fujita, K. Nakajima, and Y. Hosoya, New Type of IF-High Strength Steel with Superior Anti-secondary Work Embrittlement, *ISIJ Int.*, 2001, **41**, p 1402–1410

24. S.Q. Cao, J.X. Zhang, J.S. Wu, L. Wang, and J.G. Chen, Microtexture, Grain Boundary Character Distribution, and Secondary Working Embrittlement of High Strength IF Steels, *Mater. Sci. Eng. A*, 2005, **392**(1–2), p 203–208

25. General Motors Standard, GMW 16086, Evaluation for Susceptibility to Secondary Cold Work Embrittlement and Low Temperature Impact Fractures of Ulta Low Carbon and Phosphorous Bearing Sheet Steels, August 1, 2019, Third Edition

26. Z. Marciniak, K. Kucynski, and T. Pokora, Influence of the Plastic Properties of a Material on the Forming Limit Diagram for Sheet Metal in Tension, *Int. J. Mech. Sci.*, 1973, **15**, p 789–805

27. W.L. Server, General Yielding of Charpy-V notch and Precracked Charpy Specimens, *Trans. ASME J. Eng. Mater. Technol.*, 1978, **100**(4), p 183–188

28. D.J.F. Ewing, Calculation of the Bending of Rigid/Plastic Notched Bars, *J. Mech. Phys. Solids*, 1968, **16**, p 205–213

29. W.F. Brown, Jr. and J.E. Srawley, Plane Strain Crack Toughness Testing of High Strength Metallic Materials, *ASTM STP No. 410,* 1966

30. R.W. Hertzberg and R.H. Goodenow, Fracture Toughness and Fatigue Crack Propagation in Hot Rolled Microalloyed Steel, in *Proceedings of an International Symposium on High Strength Low-Alloy Steels, MicroAlloying, Washington, DC*, vol 75, 1975